UC-411
LBL-27884
Preprint

Lawrence Berkeley Laboratory
UNIVERSITY OF CALIFORNIA

Accelerator & Fusion Research Division

Center for X-Ray Optics

Submitted to Journal of X-Ray Science and Technology

Design and Characterization of X-Ray Multilayer Analyzers for the 50–1000 eV Region

B.L. Henke, E.M. Gullikson, J. Kerner,
A.L. Oren, and R.L. Blake

October 1989

For Reference

Not to be taken from this room

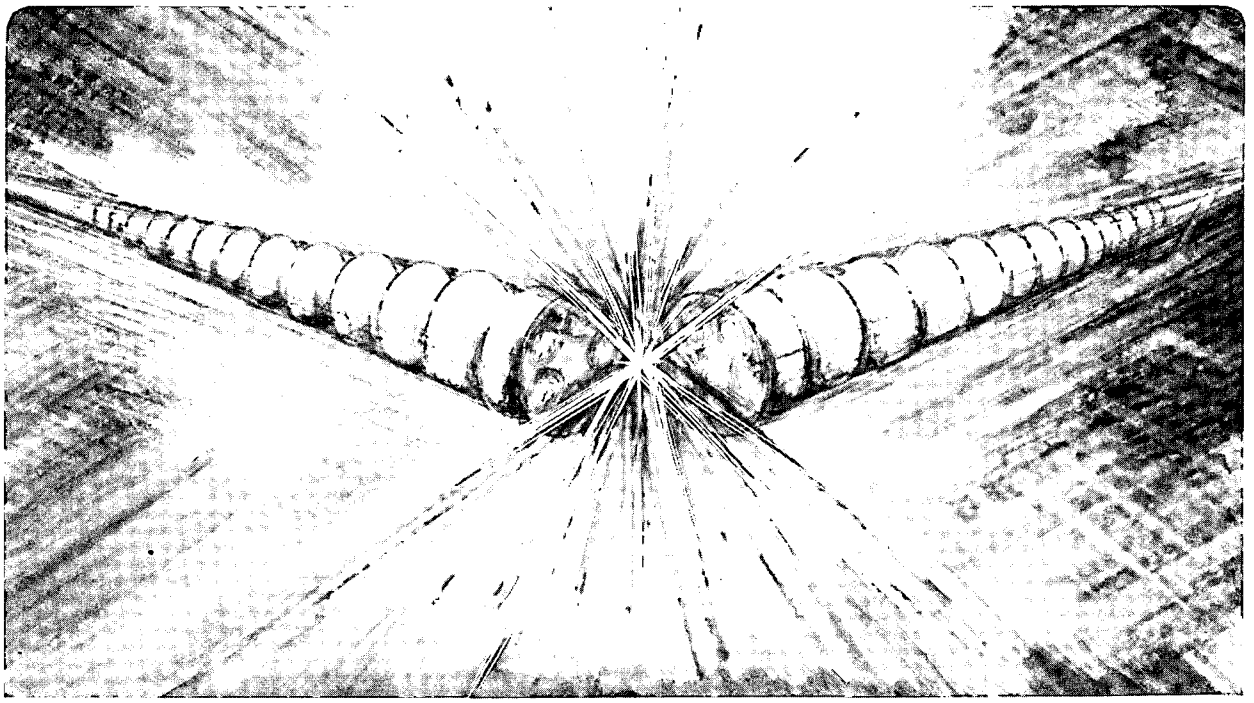

LBL-27884
Copy 1
Bldg. 50 Library.

Prepared for the U.S. Department of Energy under Contract Number DE-AC03-76SF00098.

DISCLAIMER

This document was prepared as an account of work sponsored by the United States Government. While this document is believed to contain correct information, neither the United States Government nor any agency thereof, nor the Regents of the University of California, nor any of their employees, makes any warranty, express or implied, or assumes any legal responsibility for the accuracy, completeness, or usefulness of any information, apparatus, product, or process disclosed, or represents that its use would not infringe privately owned rights. Reference herein to any specific commercial product, process, or service by its trade name, trademark, manufacturer, or otherwise, does not necessarily constitute or imply its endorsement, recommendation, or favoring by the United States Government or any agency thereof, or the Regents of the University of California. The views and opinions of authors expressed herein do not necessarily state or reflect those of the United States Government or any agency thereof or the Regents of the University of California.

DESIGN AND CHARACTERIZATION OF X-RAY MULTILAYER ANALYZERS FOR THE 50-1000 eV REGION

B.L. Henke[1], E.M. Gullikson, J. Kerner[2] and A.L. Oren[3]
Center for X-Ray Optics
Accelerator and Fusion Research Division
Lawrence Berkeley Laboratory
1 Cyclotron Rd.
Berkeley, CA 94720

R.L. Blake
Los Alamos National Laboratory, P-14
P.O. Box 1663, MS D410
Los Alamos, NM 87545

ABSTRACT

This report describes a synthesis of more than ten years of this program's development and application of multilayer analyzers for absolute Bragg spectrometry in the low-energy x-ray region of 50-1000 eV. Multilayers, defined here as systems of periodic layered structures parallel to the analyzer surface have been applied principally in the diagnostics and application of the new, intense sources of synchrotron and high-temperature plasma x radiation. Detailed absolute reflectivity characterizations are presented for selected examples of these multilayers which have been semi-empirically determined for Mica, KAP and the fabricated Langmuir-Blodgett and sputtered multilayer analyzers with d-spacings in the 10-200 Å range. Design requirements for absolute spectrometry are established. Efficient analytical multilayer reflectivity models are derived and parameterized (based upon a modification of the Darwin-Prins model for the low-energy x-ray region) -- including, for the sputtered multilayers, parameters for defining interface structure. The dependence of the reflectivity characteristics, high-order Bragg diffraction suppression, and over-all efficiency upon the model parameters is analyzed. A special spectrograph and procedure for the absolute measurement of the relevant reflectivity characteristics are described. Detailed measurements and semi-empirical characterizations are presented. Programs for small laboratory computers have been developed that allow rapid and flexible spectral analysis, transforming measured spectra to absolute spectra.

[1]LBL Emeritus, 1200 Mira Mar Ave., No. 1324, Medford, OR 97504.

[2]U.S. Dept. of Commerce, Natl. Inst. of Standards and Technology, Bldg. 221 Rm. A251, Gaithersburg, MD 20899.

[3]Dept. of Physics, B-019, Univ. of Calif. at San Diego, La Jolla, CA 92093.

CONTENTS

I. INTRODUCTION

II. DESIGN REQUIREMENTS FOR ABSOLUTE SPECTROMETRY

III. ANALYTICAL MODELS FOR MULTILAYER ANALYZERS

A. Reflection from a Single Layer of Atoms or Unit Cells; Defining the Atomic Scattering Factor, f, and the Unit Cell Structure Factor, F

B. The Modified Darwin-Prins (MDP) Model

C. The Lorentzian Approximation to the MDP Diffraction Line Profile

D. The Mosaic Multilayer Model

E. Determination and Parameterization of MF for Multilayer Systems

1. MF for Natural Crystal Multilayers

2. MF for Sputtered-or-Evaporated Multilayers

(a) Sharp Interface ($T_1 = T_2 = 0$)

(b) Compound Interface ($T_1 = T_2 = T$)

(c) Symmetrical Linear Transition Interface ($T_1 = T_2 = T$)

(d) Asymmetrical Linear Transition Interface ($T_1 \neq T_2$)

F . Predicted Effects of MF-Parameters upon Multilayer Reflectivity

1. Suppression of Higher diffraction Orders for $T_1 = T_2$

2. Suppression of Higher Diffraction Orders for $T_1 \neq T_2$

3. Summarizing the Effects of Sputtered-or-Evaporated Multilayer Structure upon Reflectivity

IV. MEASUREMENT OF MULTILAYER REFLECTIVITY

V. SEMI-EMPIRICAL MODELING FOR MULTILAYER CHARACTERIZATION

A. Determination of the Absolute d-Spacing

B. Fitting MF for Natural Crystal and Langmuir-Blodgett Multilayer Characterization

C. Fitting MF for Sputtered Multilayer Characterization

VI. APPLICATION FOR ABSOLUTE SPECTROMETRY

A. Detailed Characterizations for Selected Multilayers for the 50-1000 eV Region

B. Absolute Spectrometry

APPENDICES:

A - Form Factor Correction for f_1

B - Finite Crystal, Modified Darwin-Prins Model

C - Characterizing the Low-Angle Reflection and Diffraction of Multilayers

D - The Kinematical (with Absorption) Multilayer Model: The Lorentzian Approximation

E - Determination of the One-Dimensional Crystal Structure

F - The Langmuir-Blodgett Multilayer: Construction and Structure Determination

G - Construction of the Sputtered Multilayer

DESIGN AND CHARACTERIZATION OF X-RAY MULTILAYER ANALYZERS FOR THE 50-1000 eV REGION

B. L. Henke, E. M. Gullikson, J. Kerner and A. L. Oren

Center for X-Ray Optics
Accelerator and Fusion Research Division
Lawrence Berkeley Laboratory
1 Cyclotron Rd.
Berkeley, CA 94720

R. L. Blake
Los Alamos National Laboratory, P-14
P.O. Box 1663, MS D410
Los Alamos, NM 87545

I. INTRODUCTION

Low energy x-ray physics and its technology have been advanced considerably in the last decade as a result of the development and application of new synchrotron, high temperature plasma and now x-ray laser sources of high intensity x-ray radiation. These have important modern applications, for example, in the material sciences (physical and chemical structure analysis, x-ray microscopy, micro-radiography, micro-lithography) and in the quest for fusion energy.[1-5] Along with these developments has arisen a considerable special need for accurate, absolute x-ray spectrometry, particularly in the technically difficult soft x-ray measurement region of 50-1000 eV (10-200 Å wavelength range).

In this report we describe the design and characterization of an important group of x-ray analyzers that can be effectively applied in this low energy x-ray region of 50-1000 eV and which utilize a multiple beam interference (Bragg reflection) from a periodic system of layered structures that are parallel to the analyzer surface. We define this type of analyzer as a <u>multilayer</u> (see Fig. 1). X radiation of wavelength λ will reflect at approximately the angle θ_o, according to the well known Bragg equation:

$$m\lambda = 2d\sin\theta_o \tag{1}$$

in which d is the spacing between layers and the integer, m, is the diffraction order. As will be shown later, the actual diffraction peak positions will be at angles slightly larger than those predicted by (1) because of refraction. For x rays the

refractive index is less than unity by the unit decrement optical constants δ and β, and given by the relation, $n = 1-\delta-i\beta$. For the low energy region, the constants δ and β (where β introduces the effect of absorption), are considerably larger than those for the conventional x-ray region.

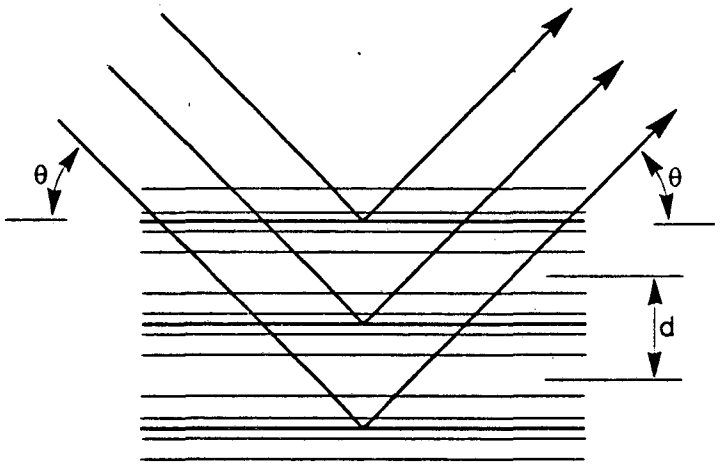

XBL 894-6201

1. Defining the multilayer: A periodic system of layered structures that establish characteristic groups or "cells" of atomic reflecting planes that are parallel to the multilayer surface. Analyzer reflectivity is thus simply determined by the one-dimensional distribution of the scattering atoms within the cell.

The diffraction "lines" will be broadened as the number of layers which contribute to the multiple beam interference is limited by absorption within the analyzer. Elementary optical principles suggest that the energy and wavelength resolutions may be estimated by the relation:

$$\left|\frac{\Delta\lambda}{\lambda}\right| = \left|\frac{\Delta E}{E}\right| = \frac{1}{mN_{eff}} \tag{2}$$

where N_{eff} is the effective number of reflecting layers. $N_{eff}d$ is then an effective depth and $2N_{eff}d/\sin\theta$ is a pathlength within the multilayer and which we may set proportional to the mean absorption pathlength, $1/\mu$. Here μ is the linear absorption coefficient and is related to β of the multilayer by $\beta = \mu\lambda/4\pi$. Combining this relation for $\Delta\lambda/\lambda$ with that obtained by differentiating the Bragg relation (1), we obtain a relationship for $\Delta\theta$, the angular width of the broadened diffraction "line":

$$\Delta\theta = \left|\frac{\Delta\lambda}{\lambda}\right| \tan\theta = \frac{\tan\theta}{mN_{eff}} \sim \frac{2\mu d}{m\cos\theta} \tag{3}$$

This relationship of the multilayer's diffraction line width to absorption is rigorously established in Sect. III for a system of parallel and ordered reflecting layers for the low energy x-ray region.

The required d-spacings for soft x-ray analyzers must be in the 10-200 Å range. Over the past ten years we have successfully applied several types of practical multilayers with large d-spacings for absolute x-ray spectrometry in the areas of materials analysis and the diagnostics of laser-produced plasmas[6,7]. Examples of these multilayer analyzers are: (1) the natural crystals, mica and the acid phthalates (cleavage plane spacings of approximately 10 and 13 Å respectively); (2) the molecular multilayers of the Langmuir-Blodgett type (d-spacings in the 35-80 Å range); and (3) the sputtered-or-evaporated multilayers (d-spacings in the 20-200 Å range). All of these multilayers can be mounted in sufficiently thin sections to be used for curved, focussing optics.[8]

In Sect. II we define the appropriate measurement parameters for characterizing multilayer reflectivity and we discuss some of the basic design requirements for the application of multilayers for optimized absolute spectrometry. In Sect. III we introduce new and efficient analytical descriptions for low energy x-ray multilayer analyzer reflectivity, establishing the appropriate material parameters that determine reflectivity. In Sect. IV we describe the experimental procedures that are applied in this laboratory for the absolute measurement of multilayer reflectivity. We then, in Sect. V, combine our analytical and experimental descriptions to obtain semi-empirical, detailed characterizations of practical multilayer analyzers which are representative of the natural crystal and of the synthesized Langmuir-Blodgett and sputtered multilayer systems. Finally we present in Sect. VI comparisons of the reflectivity characteristics of these multilayer types when optimally applied in the 50-1000 eV region.

II. DESIGN REQUIREMENTS FOR ABSOLUTE SPECTROMETRY

Plotted in Fig. 2 is the reflected intensity of low energy x radiation (930 eV/13.3 Å) vs reflection angle, θ, for a tungsten-carbon multilayer showing both the first order diffraction ($\theta \approx 11°$) and the low angle, "total reflection" region. This response was predicted using the analytical modified Darwin-Prins model developed in Sect. III and for a

multilayer of 100 layer pairs with 14 Å of W and 21 Å of C (assuming sharply defined interfaces). Also defined here are the reflectivity parameters that determine the absolute characteristics of a spectral line analysis. θ, P, R and ω are the position, peak reflectivity (reflected fraction of incident intensity), integrated reflectivity (usually given here in milliradians--mr) and full-width-at-half-maximum (FWHM) of a given diffraction line. Also defined here is θ_c which measures the extent of the Fresnel "specular" reflection region (angle for half-total-reflection-intensity, $I_o/2$). For a given line shape, R is proportional to ωP. Usually, low energy multilayer diffraction lines are well approximated by a Lorentzian for which $R = (\pi/2)\omega P$ (established in Sect. III). As is suggested in Fig. 3, the spectrometric signal is determined by the peak reflectivity, P, when the incident beam collimation, $\Delta\phi$, is sharp compared to the FWHM, ω; however, this signal is determined by the integrated reflectivity, R, when the collimation angular width embraces the total diffraction line. Specifically, for incident x radiation of i_o photons/stearadian from a small source region which is sharply collimated by $\Delta\phi = \Delta\theta_s$ in the reflection plane and by ψ in the oblique directions, the number of photons reflected is given by:

$$N_x = i_o \psi P \Delta\theta_s \tag{4}$$

and with broad collimation the number of photons reflected is given by:

$$N_x = \int I(\theta)\, d\theta = i_o \psi R \tag{5}$$

In (4) and (5), we are neglecting the possible contributions of background radiation.

The quality of a spectral line measurement is usually strongly affected by the presence of background radiation. This background may be effectively an extension of the reflection "tail" resulting from the specular reflection of low energy x radiation present in the source along with that of the diffusely scattered radiation from structures on the surfaces of the optical elements, the analyzer and collimating system. (Usually for the low energy x rays, fluorescent radiation from these surfaces contributes negligible background.) [Note: as will be discussed below, it is important to define the parameters ω, P and R for our analytical modeling as well as for our experimental measurement of the diffraction line profile <u>after</u> a background subtraction has been made.]

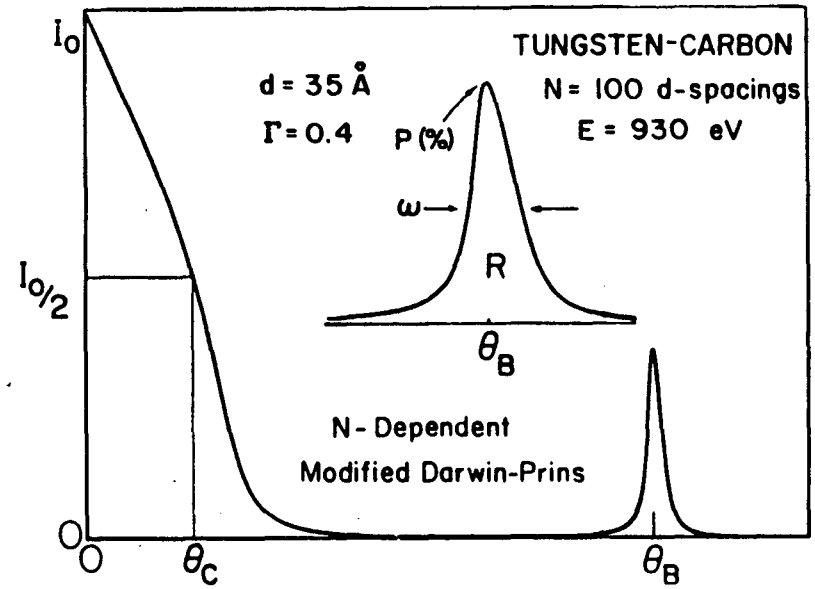

XBL 894-1611

2. A multilayer reflectivity curve, $I(\theta)$, (fractional intensity reflected at angle θ) including the small-angle "total" reflection region and the first order diffraction "line" calculated using the modified Darwin-Prins (MDP) model developed in Sect. III. For a Tungsten-Carbon system of 100 layer-pairs of 14 Å-W and 21 Å-C with assumed sharp interfaces and for incident 930 eV/13.3 Å x radiation. Defined here are the spectral characteristics: θ_c, the critical angle for total reflection (at $I_o/2$ intensity); θ_B, the diffraction line position; R, the integrated reflectivity (area within the diffraction "line" relative intensity profile, $I(\theta)$); P, the relative peak intensity; and ω, the full-width-at-half-maximum (FWHM) angular width.

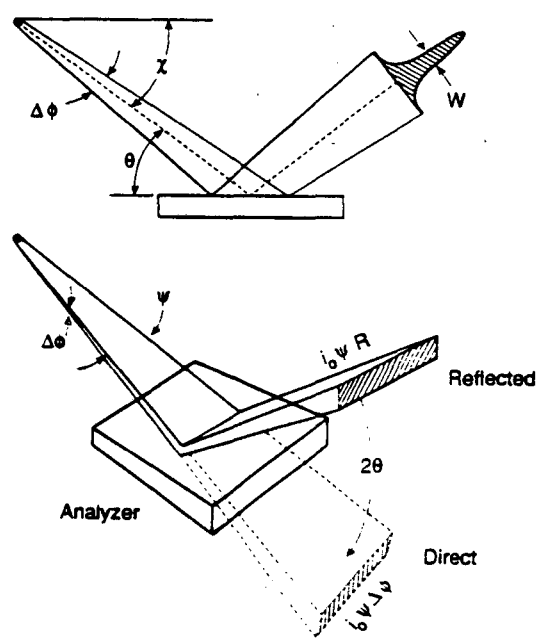

3. The geometry that determines the "signal" (total no. of photons reflected at the diffraction line position for a small source of i_o photons/stearadian with collimation of $\Delta\phi$ in the reflection plane and ψ in the plane normal to the reflection plane. Illustrated schematically here are the two collimation limits: $\Delta\phi = \Delta\theta_s$ for sharp collimation, within the peak of the diffraction profile and $\Delta\phi = \Delta\theta_b$ for broad collimation, embracing essentially the total diffraction line.

XBL 894-6200A

The statistical precision of a spectral line measurement is determined in part by the ratio of this signal to the associated background radiation and it is therefore required that this background be minimized when possible by the design of the spectrometry. This is accomplished by choosing a multilayer d-spacing that allows the spectral lines to be measured in the large-angle region where the "tail" of the low-angle reflected/scattered background is either negligible or accurately accountable.

Another important advantage of applying multilayer analyzers in the larger angle region is that in this way the product of its resolving power, $\lambda/\Delta\lambda$, and the "signal" (the number of photons reflected to the detector within a diffraction line) will be maximized. This quantity may be generally considered as an important "Figure of Merit." Using relations noted above, we may obtain a good estimate of this quantity, for broad collimation, as follows:

$$\left(\frac{\lambda}{\Delta\lambda}\right) i_o \psi R = m N_{eff} i_o \psi R \sim \frac{m \sin\theta}{2\mu d} i_o \psi R \sim \frac{i_o \psi R}{\mu\lambda} \sin^2\theta \tag{6}$$

Therefore, for the measurement of a given wavelength, λ, it is important to maximize the quantity $R\sin^2(\theta)/\mu$.

In summary, we need, for optimized spectral analysis, to choose a multilayer with a d-spacing that allows large angle spectroscopy (typically in the 10°–80° range) in order to maximize signal and signal-to-background. It is also essential, for optimized spectral analysis, to have a multilayer analyzer of the required resolution with the highest attainable associated integrated reflectivity, R.

In the following, Sect. III, we present relatively simple and accurate analytical models for the prediction of the spectrometric parameters R, ω, P and θ_c and their dependence upon the structure and composition of a given multilayer analyzer.

III. ANALYTICAL MODELS FOR MULTILAYER ANALYZERS

Macroscopically, a multilayer analyzer may be described as a system of heavily and lightly scattering layered regions with a periodicity spacing, d, approximately equal to the wavelength to be analyzed. The simplest of such systems is a sputtered-or-evaporated set of perfectly spaced and uniform pairs of "heavy" and "light" layers with sharp interfaces. Layer spacing and analyzed wavelengths are to be sufficiently large compared to atomic and other fluctuations in electron density to permit description by macroscopic optical constants. For such a

long wavelength analyzer, each layered region can be accurately characterized by the optical constants, δ and β, which define the refractive index, n ($= 1-\delta-i\beta$). For theoretically modeling such a system, it has been conventional to apply optical E&M (OEM) solutions, e.g. by successive applications of the Fresnel reflection equations at each interface. Computer programs for OEM modeling have been developed and made available at this and other laboratories which also allow descriptions of "soft" interfaces by using "stepped" sub-layered interface profiles [9,10,11]. These modeling procedures originally evolved from optical interference filter technology.

Presented here is an analytical model of the multilayer analyzer which we have recently introduced [12] that is based upon the calculation of reflected amplitude by summing the amplitudes scattered from the atoms comprising the multilayer structure. We have used a modified Darwin-Prins crystallographic description that can now be applied accurately in the low energy x-ray region.

This "microscopic" description, complementary to that of the OEM approach, has several important advantages: (1) as the wavelengths approach atomic dimensions, the atomic diffraction contributions have an angle-dependence which may be simply included in the atomic scattering description as a <u>form-factor correction</u> (described below); (2) more precise criteria may be defined for the allowable extent of layer inhomogeneities in the practical multilayer system that can be tolerated in a given model description; and finally, (3) this approach yields relatively simple, analytical models that permit flexible and rapid multilayer reflectivity prediction with a small laboratory computer.

We begin our development with a review of the basic description of the reflection of x rays from planes of atoms, following the approaches presented in the excellent classic texts, *The Optical Principles of the Diffraction of X-Rays* by James and *X-Rays in Theory and Practice* by Compton and Allison.[13,14]

A. Reflection from a Single Layer of Atoms or Unit Cells; Defining the Atomic Scattering Factor, <u>f</u>, and the Unit Cell Structure Factor, <u>F</u>

We describe first the amplitude that is reflected from an elementary plane of atoms irradiated by a <u>parallel</u> beam of x rays. The magnitude of the reflected amplitude at a finite position, B, can be most readily obtained by summing the amplitudes from the Fresnel half-period zones around a central point, P, as depicted in Fig. 4. These zones are bounded by the loci of points for which the path difference to B is $n\lambda/2$ greater

than that for the central ray, APB. The integer order number, n, of these loci specifies a set of ellipses with major and minor axes, a_n and b_n given by:

$$a_n = \frac{\sqrt{n\lambda r}}{sin\theta}, \quad b_n = \sqrt{n\lambda r} \tag{7}$$

where r is the distance PB. The area of each annulus is nearly equal to the area of the central elliptical zone. However, as the major and minor axes, a_n and b_n, of the successive zones increase, the mean scattered amplitude of the atoms involved decreases because the mean pathlength and obliquity increase (see Compton and Allison [14]). The relative direction of the decreasing resultant amplitude vectors from each zone will reverse for each successive half-period zone, resulting in a summed amplitude that simply approaches one-half that from the central zone (depicted in Fig. 4). The amplitude reflected to point B from the central zone may be obtained by summing the scattered waves from the individual points taking into account their phase relative to P, which yields the product $\underline{-i2/\pi}$ times the sum of the amplitudes scattered by the individual atoms in the zone. The phase shift upon reflection from this central zone is found to be 90 deg behind that from point P, this shift is in addition to any phase shift in the wave scattered from a single atom, A. Using (7) yields the net scattered amplitude at B,

$$-imA\frac{r\lambda}{\sin\theta} \tag{8}$$

where m is the number of atoms per unit area and A is the amplitude scattered per atom and is given below using the <u>atomic scattering factors</u>. If the atomic plane is comprised of different atoms, with m_q atoms per unit area of type q, of scattering amplitude A_q, we would replace mA in (8) by $\sum m_q A_q$.

If the atomic plane is not perfectly uniform but instead includes inhomogeneities (e.g. "holes" or fluctuations in atomic density), an average value of m may be used to accurately yield the reflected amplitude <u>provided</u> that the dimensions of the inhomogeneities are small compared to those of the Fresnel zones effective in the reflection (approximately equal to $\pi a_1 b_1$). This criterion can be useful in the modeling of rough or diffused interfaces, as will be discussed later in this Section.

4. Geometry for determining the amplitude reflected from an atomic plane using the Fresnel half-period zone construction. The pathlength to B from a point source at A and scattering from the elliptical loci of points in the plane of the nth ellipse is $n\lambda/2$ greater than that reflected from the central point at P. The amplitude reflected from each successive annular zone (between ellipses) may be described as a vector that reverses in direction for each successive zone and slowly decreases with n (as the average angle, θ, and the average distance to a point within the nth annulus increases). The total amplitude from all zones thus approaches one-half of that which is reflected from the central, elliptical zone as suggested in the vector summation diagram.

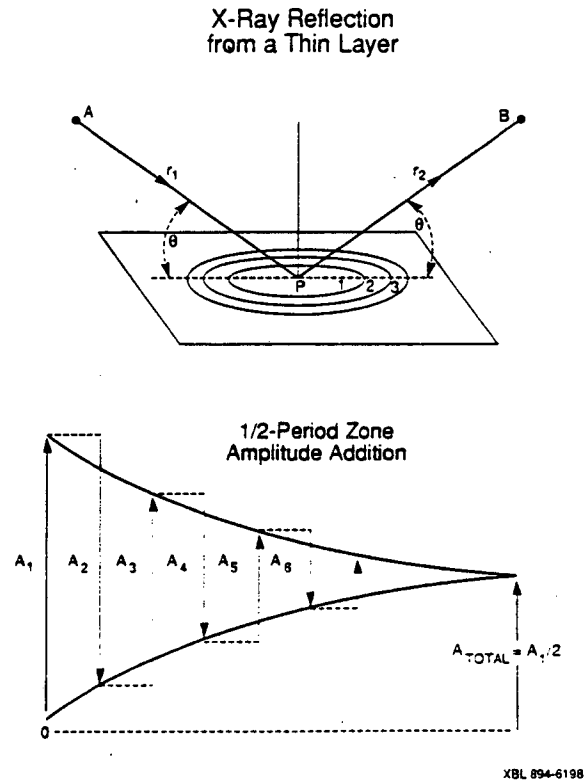

For reflection from a composite layer of m_q atoms per unit area of type q, the scattered amplitude is

$$-i\left(\sum_q m_q A_q\right)\frac{r\lambda}{\sin\theta} \tag{9}$$

For the multilayer analyzer, as suggested above, the reflection and absorption for each periodic layer (unit group of atomic layers) must be small in order to provide a sufficiently large number of effective reflecting planes to yield the desired spectrometric resolution. We may therefore efficiently describe the reflection of a multilayer as the sum of the reflections from the periodic, characteristic thin group of layers or "cells." Within such a single thin layer set we assume that the incident intensity is essentially the same for each plane of atoms and that we can neglect any multiple reflections within the unit cell thickness (thus using a kinematical description) and obtain the total amplitude as summed for all the atomic planes within this repeated group or cell:

$$-i\left[\sum_q m_q A_q \exp\left(-i4\pi\frac{z_q}{\lambda}\sin\theta\right)\right]\frac{r\lambda}{\sin\theta} \tag{10}$$

in which z_q is the distance of the q-type atoms from a reference plane, and $4\pi z_q \sin\theta/\lambda$ is the phase shift from the phase of the reflected amplitude off the reference plane.

The needed parameter, A_q, which is the amplitude scattered per atom, is defined as proportional to a complex, dimensionless factor, the <u>atomic scattering factor</u> as noted in Fig. 5. Here r_o is the classical electron radius, and the polarization factor $P(2\theta)$ is equal to unity if the incident electric field amplitude, A_o, is perpendicular to the plane of reflection, and equal to $\cos(2\theta)$ if in the plane of reflection. Often, for highly polarized x radiation (e.g., with synchrotron radiation) only one component need be considered. For unpolarized x radiation (e.g., from an x-ray tube anode or a fluorescer) both components would need to be considered.

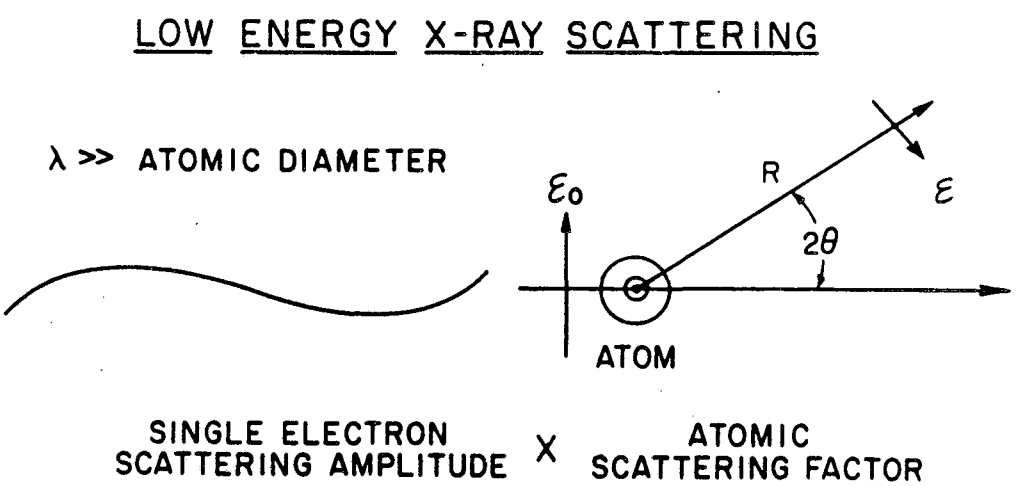

5. Defining the atomic scattering factor, f (= f_1+if_2). For wavelengths that are large compared to atomic dimensions, the amplitude scattered at distance R is equal to that scattered by a free electron multiplied by a dimensionless, complex <u>atomic scattering factor</u>. Here r_o is the classical electron radius and $P(2\theta)$ is the polarization factor, equal to cos 2θ for the incident electric vector in the scattering plane (as shown) and equal to unity when E_o is perpendicular to this plane.

This atomic scattering factor f (= f_1+if_2), is <u>independent</u> of angle θ, for wavelengths which are large as compared to atomic dimensions (Rayleigh scattering). When diffraction by the atomic electron "cloud" introduces an angle dependence (when $\sin(2\theta)/\lambda > 0.1$) we may simply correct f by reducing the f_1 component by an

amount, Δf_o, given by:

$$\Delta f_o = Z - f_o \tag{11}$$

where f_o is the well tabulated angle dependent <u>form factor</u> [15] given vs $\sin(2\theta)/\lambda$, and Z is the atomic number for the particular atom. The satisfactory accuracy of this simple correction for f in the region of large angles and shorter wavelengths is demonstrated in Appendix A.

For a particular atom and for the low energy region of interest here, the atomic scattering factor can vary considerably with photon energy as a result of <u>anomalous dispersion</u>. In order to achieve accurate modeling of low energy x-ray interactions we have calculated the atomic scattering factors of 94 elements for the photon energy region of 100-2000 eV.[16] We are now updating these tables which are based semi-empirically upon the current theoretical and experimental data bases of photoabsorption cross sections (using a Kramers-Kronig formulation), for an extended energy region of 50-10,000 eV[17].

Finally, we may combine these results given above to obtain the fractions of the incident amplitude that are reflected, $-is$, and transmitted, $1-i\sigma$, by a layer of <u>M</u> unit cells per unit area. As noted in Fig. 6, the fractional amplitude that is reflected is defined by:

$$-s = r_o\lambda\frac{MF(\theta)}{\sin\theta}P(2\theta) \tag{12}$$

and the fractional amplitude transmitted is defined by:

$$-\sigma = r_o\lambda\frac{MF(0)}{\sin\theta} \tag{13}$$

in which we introduce the layer's <u>structure factor per unit area, MF</u> = MF_1+iMF_2, given by:

$$\begin{aligned} MF_1 &= \sum_q m_q[f_{1q}\cos\phi z_q + f_{2q}\sin\phi z_q] \\ MF_2 &= \sum_q m_q[f_{2q}\cos\phi z_q - f_{1q}\sin\phi z_q] \end{aligned} \tag{14}$$

for a distribution of m_q atoms per unit area of species-q and atomic scattering factor f_q (= $f_{1q}+if_{2q}$) located at distance z_q from a reference plane. The phase factor, ϕ, is equal to $4\pi\sin(\theta)/\lambda$.

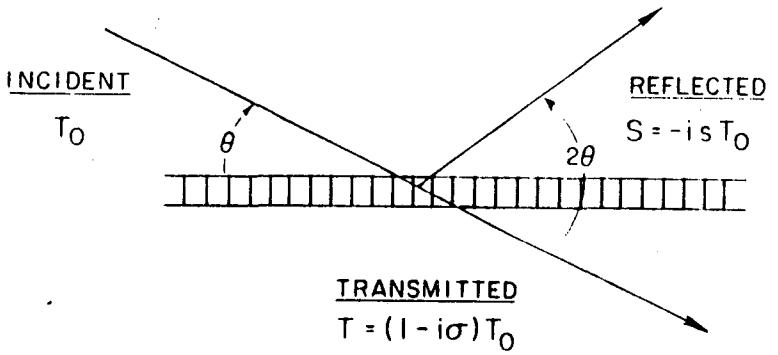

FOR M UNIT CELLS/UNIT AREA OF STRUCTURE FACTOR, $F_1 + iF_2$, AND OF AVERAGE ATOMIC SCATTERING FACTOR, $\bar{f}_1 + i\bar{f}_2 = F_1(0) + iF_2(0)$

$$-\sigma = r_0\lambda \frac{MF_1(0) + iMF_2(0)}{\sin\theta} \quad \text{AND} \quad -s = r_0\lambda \frac{MF_1(0) + iMF_2(0)}{\sin\theta} P(2\theta)$$

$P(2\theta) = 1$ OR $\cos 2\theta$ FOR THE TWO POLARIZED COMPONENTS

XBL 894-1612

6. The fractional amplitude that is reflected, $-is$, and that transmitted, $1-i\sigma$, kinematically by a thin group or cell of atomic planes characterized by its structure factor per unit area, MF. $F = F_1(\theta) + iF_2(\theta)$, is the unit cell structure factor and M is the number of unit cells per unit area.

If the distribution of the atoms within the unit cell can be treated as continuous (e.g. for sputtered or evaporated multilayers), the structure factor per unit area, MF, may be defined by the following integral equivalent of (14):

$$MF = \sum_q \int_o^d n_q(z) f_q \exp(-i\phi z)\, dz \tag{15}$$

for a distribution of $n_q(z)$ atoms per unit volume of species-q, where z is measured from a reference plane. When (15) is expanded to determine its real and imaginary parts, MF_1 and MF_2, both the cosine and sine terms are involved as in (14) except when z is measured from a symmetry plane of the unit cell which allows the sine terms to drop out of (14) and (15).

Note: for the calculation of the transmitted amplitude by the layer of unit cells, we are concerned only with scattering in the forward direction, $\theta = 0°$, and therefore have introduced F(0) into (13) which is the value of $F(\theta)$ as θ approaches zero. Hence the reflection and the transmission of a single layer (or, as shown below, for the multilayer) depends upon its composition, density and structure simply through the quantity MF, as defined

here in (14) and (15).

B. The Modified Darwin-Prins Model

We outline next the development of a dynamical analytical model for the reflection of low energy x rays by a multilayer analyzer with N parallel layered structures, each scattering in proportion to its structure factor per unit area, MF, as described above. We modify the approach used by Darwin and Prins that describes crystal reflection for the conventional x-ray region.

In the dynamical description of the propagation of waves through the multilayer all possible multiple reflections within the layers must be taken into account in order to describe the net downward propagating wave amplitude, T, and the net upward propagating wave amplitude, S. This accounting originally was elegantly accomplished by Darwin in his solution of the self-consistent difference equations describing the process for any two adjacent layers within a non-absorbing semi-infinite multilayer. (Prins introduced the effects of absorption by the formal substitution of complex atomic scattering factors and a complex refractive index for the crystal's corresponding real values assumed by Darwin in his original solution which neglected absorption.) The resulting difference equations are presented in Fig. 7.

Dynamical Reflection and Transmission

T_r and S_r are total downward and upward amplitudes at the rth layer of a large slab

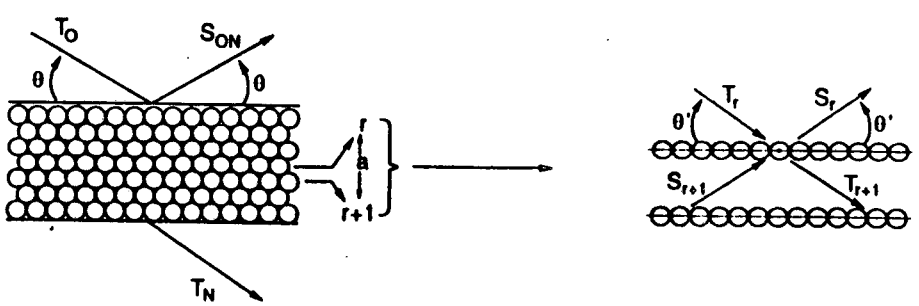

Difference Equations

$$S_r = -is\,T_r + (1-i\sigma)e^{-i\delta}S_{r+1}$$
$$T_{r+1} = (1-i\sigma)e^{-i\delta}T_r - ise^{-2i\delta}S_{r+1}$$

XBL 894-6215

7. The self-consistent difference equations, the solution of which leads to the Darwin-Prins dynamical reflectivity equation for the semi-infinite multilayer, S_O/T_O, given in (16). (δ is the phase shift for the path between layers, $2\pi d\sin\theta/\lambda$.) See, for example, Appendix D for a solution of these equations for the kinematical reflectivity from an absorbing semi-infinite multilayer.

This approach yields an analytical result for the ratio of the reflected to the incident amplitudes, S_o/T_o, at the surface of the semi-infinite multilayer which is given by:

$$S_o/T_o = \frac{-s}{(\sigma+\xi) \mp \sqrt{(\sigma+\xi)^2 - s^2}} \tag{16}$$

The new parameter, ξ, introduced in this result, is defined by:

$$\xi = \frac{2\pi d}{\lambda}(\sin\theta - \sin\theta_o) \tag{17}$$

where, as discussed below, $\sin\theta_o$ effectively defines a "region of interest" around a particular diffraction line and is given by the Bragg equation, $m\lambda = 2d\sin\theta_o$. Now, in this Darwin-Prins (DP) difference equation solution, it is established that the net downward propagating wave at the Nth layer has an amplitude given simply by $T_o x^N$, where x is defined by:

$$x = (-1)^m \exp(-\eta) \text{ and } \eta = \mp\sqrt{s^2 - (\sigma+\xi)^2} \tag{18}$$

The value of x includes the contributing effects of all possible multiple reflections within the semi-infinite multilayer. (The + or - sign is chosen so as to have the real part of η be positive.) Using this result, we derive (in Appendix B), a modifying factor which converts the reflected amplitude ratio, S_o/T_o, given in (16) to the amplitude reflection ratio, S_{oN}/T_o, for a finite multilayer of N layers. The resulting equation is:

$$S_{oN}/T_o = S_o/T_o \left[\frac{1 - x^{2N}}{1 - (S_o/T_o)^2 x^{2N}}\right] \tag{19}$$

Note: The N-dependent modifying factor (in brackets) must, of course, approach unity as N becomes large. It is often of practical importance in the construction of optimized multilayers to determine the number of layers to be deposited for which this factor is equal to about 0.95 for the required energy range of application.

Also derived in Appendix B is the amplitude ratio, T_{oN}/T_o, that is transmitted through the N layer system. This is given

by:

$$T_{oN}/T_o = \frac{[1-(S_o/T_o)^2]x^N}{1-(S_o/T_o)^2 x^{2N}} \tag{20}$$

In the usual way, the intensity ratio that is reflected or transmitted for unpolarized incident x radiation (e.g. x-ray tube radiation) is obtained by taking one-half of the sum of the moduli squared of the two polarization component amplitudes as obtained from Eq. (19) and (20), by setting $P(2\theta)$ equal to unity and to $\cos(2\theta)$ in the reflected amplitude, s, of equation (12). For polarized x radiation (e.g. synchrotron radiation), the intensity ratio is equal to the sum of the moduli squared of the two components of the electric field, one for the electric vector's perpendicular component to the plane of reflection [with $P(2\theta) = 1$] and the other for this electric vector's component parallel to the plane of reflection [with $P(2\theta) = \cos(2\theta)$].

As may be easily shown, the reflected intensity will be significant only when ξ, defined in (17), is small and therefore when $\sin\theta$ approaches $\sin\theta_o$. We may rewrite (17), using the Bragg relation (1):

$$\xi = \frac{2\pi d}{\lambda}(\sin\theta - \frac{m\lambda}{2d}) \tag{21}$$

(m = 0 for the small angle, Fresnel reflection region, m = 1 for the first order diffraction line, m = 2 for the second order diffraction line, etc.) In order to apply this intensity function continuously in θ-plots for the total angular range, m is automatically set either to zero or to that integer which is nearest to the value of $(2d\sin\theta/\lambda)$ in our code.

In Appendix C it is shown tht the MDP zero-order prediction for the reflected amplitudes at the small angles reduces identically to the Fresnel reflection description. Also, we have found that this MDP prediction for the small-angle reflectivity is generally in close agreement with that given by the OEM model as discussed below and in Appendix C.

By using a unit area structure factor, MF, calculated with the specific relations presented in Sect. V, we have applied this modified Darwin-Prins (MDP) result to obtain the ratio of the reflected intensity to that incident, $I(\theta)$, for a pure tungsten-carbon multilayer with assumed sharply defined interfaces and of d-spacing = 35 Å and with $\Gamma = 0.4$. (Γ is the ratio of thickness of the heavy element to the d-spacing for a sharp interface geometry.) A plot of $I(\theta)$ for the incident photons of Cu-L_α (930 eV/13.3 Å) which includes the small angle Fresnel region and the first order diffraction line was shown in

Fig. 2 for a number of layer pairs, N, equal to 100. This plot illustrates a satisfactory design of this W-C analyzer for the given wavelength because it places the first-order diffraction line well above the "total reflection tail" background. As discussed in Sect. II, for the larger angles of diffraction, the absorption per layer is minimized and consequently more layers participate in the reflection and higher resolution results. We show in Appendix C that when the first-order diffraction angle is larger than about three times the critical cut-off angle for "total reflection", θ_c, the magnitude of the parameters σ and s are small compared to unity, thus insuring accuracy in our MDP modeling.

As a test of the accuracy of this MDP model we compare its predictions to those of the OEM model. Equivalence of the two model calculations for long wavelength x rays is obtained by using the relations between the optical constants, δ and β, which define a uniform sublayer section of a multilayer and the atomic scattering factors of the atoms comprising the section, viz:

$$\delta = \frac{r_o \lambda^2}{2\pi} \sum_q n_q f_{1q}$$

$$\beta = \frac{r_o \lambda^2}{2\pi} \sum_q n_q f_{2q} \tag{22}$$

for a uniform region of n_q atoms per unit volume of species-q having an atomic scattering factor $f_q = f_{1q} + i f_{2q}$.

Note: This optical equivalence is definable for the low energy x-ray region only for wavelengths which are: 1) sufficiently long compared to the dimensions of the atoms so that these may be treated as "point scatters", and 2) sufficiently long as compared to fluctuations in atomic densities which otherwise may also introduce significant angle-dependent diffraction effects.

In Figs. 8 and 9 we compare the total reflection region and the first, second and third order diffraction line intensities for this W-C multilayer as calculated by the MDP model to those calculated by the optical E&M (OEM) model (dashed lines) for N = 100 and 30 in order to illustrate the equivalence of the two models in this low energy x-ray region. Similarly, we compare in Fig. 10 the intensity profiles reflected by the multilayer of N = 100 at and near normal incidence. (OEM - dashed lines.) Note: Multilayer reflection at normal incidence is of considerable current interest in the development of x-ray lasers and of reflection x-ray imaging optics.

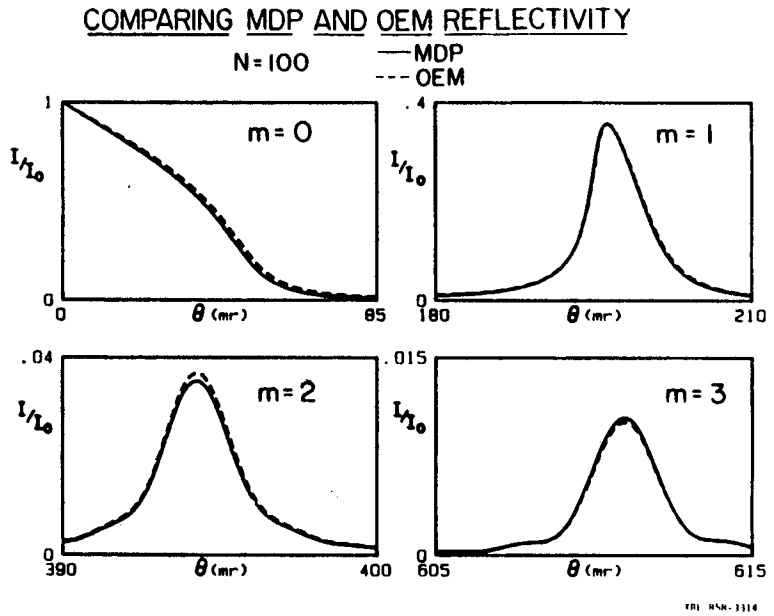

8. Illustrating the equivalence of the Modified Darwin-Prins (MDP) and the Optical E&M (OEM) descriptions for low-energy x-ray reflectivity in the small-angle total reflection region and large-angle first, second and third order diffraction line profiles. (930 eV/13.3 Å x radiation reflected from 100 layer-pairs of 14 Å -W and 21 Å -C with sharp interfaces. OEM-dashed line.)

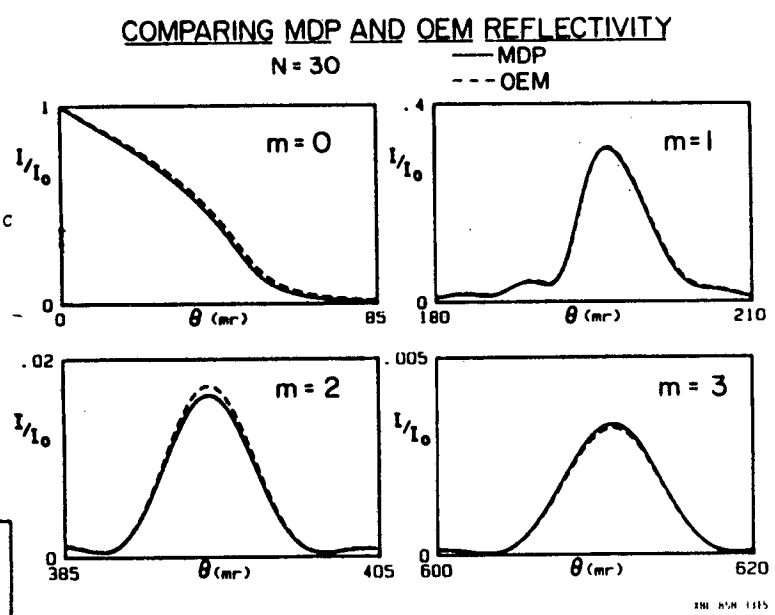

9. Similar comparisons as for Fig.8 except for a W-C multilayer with 30 layer-pairs.

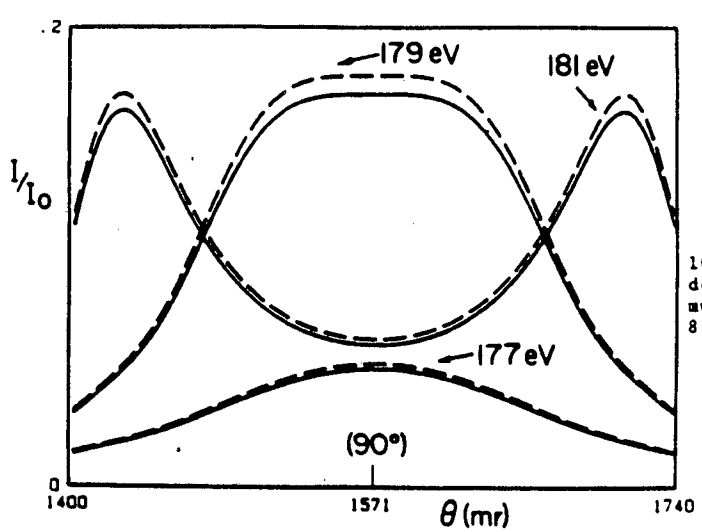

10. Illustrating the equivalence of the MDP and the OEM descriptions for near normal incidence low-energy x-ray multilayer reflectivity. (Multilayer parameters as for Fig. 8. MDP-solid line, OEM-dashed line.)

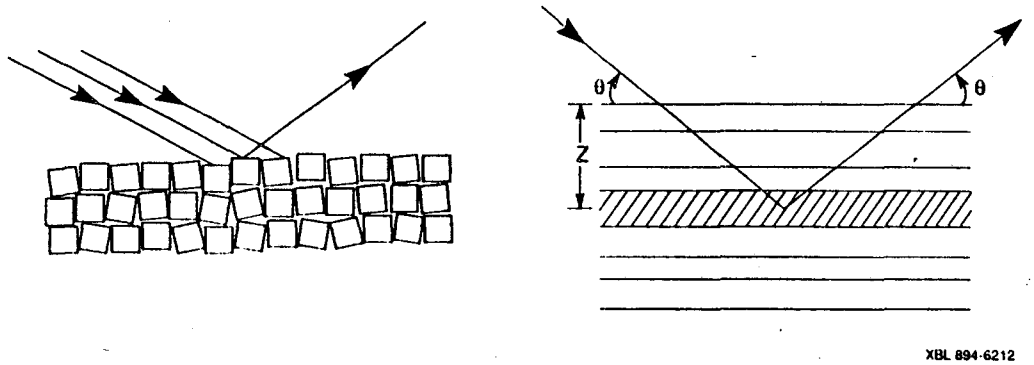

11. The Mosaic Multilayer Model. It is assumed that the mosaic multilayer is broken up into thin, ordered "crystal" segments, each reflecting coherently and kinematically but with an amplitude that has a random phase relative to those from the other segments because of a small random variation in the segment's orientation, position or d-spacing. Therefore, the total number of photons that are reflected within the reflected diffraction line from this mosaic multilayer is the sum of the angle-integrated number of photons from each thin segment reduced by the transmission factor for x rays to and from the segment, $\exp(-2\mu z/\sin\theta)$ (where z is its depth and μ is the multilayer's linear absorption coefficient). This result yields a corresponding integrated reflectivity for the mosaic multilayer, R_m, as given in (28). Illustrated here are two types of mosaic structure which may lead to this R_m.

We have developed a <u>Modified Darwin-Prins Program</u> for small laboratory computers that presents, flexibly and rapidly, for a given multilayer MF value and d-spacing: 1) the predicted intensity spectrum, $I(\theta)$, including the Fresnel low-angle reflection region and the large-angle diffraction orders (for $\theta_1 > 3\theta_c$); and 2) the predicted values versus photon energy or wavelength of θ_c, R, ω and P. In order to present the parameters R, ω and P which can be compared directly to those measured, the program calculates these from the diffraction line profiles that are generated <u>after</u> subtracting the background "tail" that passes through the intensity points at + and - 3ω from the peak position. The subtracted background is assumed to decrease as $(\sin\theta)^{-4}$ (as for the large-angle Fresnel reflection tail).

C. Lorentzian Approximation to the MDP $I(\theta)$ Distribution

For conventional x-ray reflection from crystal analyzers of relatively high perfection and low absorption, the dynamical contribution of the internally multiply reflected components to the total reflected amplitude is significant. Often, for the low energy x-ray reflection from large d-spacing analyzers of typically lower perfection and of higher absorption, an accurate and simplifying approximation to the MDP model may be obtained by neglecting this multiple reflection contribution.

In Appendix D we present a derivation of a kinematical (with absorption) model for multilayer reflectivity which we obtain by solving the difference equations defined in Fig. 7 after setting to zero the dynamical, downward reflected amplitude term in the second equation. The result for the relative reflected intensity, $I(\epsilon)$, for an unpolarized incident beam has a Lorentzian diffraction line profile given by:

$$I(\epsilon) = \frac{R_l(\omega/2\pi)}{\epsilon^2 + (\omega/2)^2} \tag{23}$$

in which ϵ is the angle measured from the refraction-shifted peak position and is equal to:

$$\epsilon = \theta - (\theta_o + \delta/\sin\theta_o \cos\theta_o) \tag{24}$$

Note: The increase in the angle of reflection because of refraction is given here as $\delta/\sin\theta_o\cos\theta_o$. This prediction of the peak shift resulting from refraction may also be obtained by combining Snell's law and the Bragg equation (eg. from (29) below), and dropping second order and higher terms in delta and beta. The diffraction line position is defined and measured in this work as the <u>centroid</u> position which is also the maximum intensity point for a symmetric line profile such as the Lorentzian. For low absorbing, well ordered crystals (with significant multiple internal reflections) the diffraction line is asymmetric and the maximum intensity position shifts slightly from that of the centroid (see for example (12) or (13)).

The peak intensity (relative to that incident), P, becomes:

$$P = I(0) = \frac{2R_l}{\pi\omega} \tag{25}$$

The FWHM, ω, is given in this approximation by;

$$\omega = \mu\lambda/2\pi \sin_o \cos\theta_o = \frac{\mu d}{\pi m \cos\theta_o} \tag{26}$$

which has the same dependence upon the multilayer's linear absorption coefficient, μ, and upon θ as predicted in the Introduction using elementary optical principles.

By integrating this Lorentzian intensity distribution we obtain for the integrated reflectivity, R_L:

$$R_l = \frac{r_o^2 \lambda^3}{2\mu d^2}[(MF_1)^2 + (MF_2)^2]\frac{(1+\cos^2 2\theta)}{2\sin 2\theta} \tag{27}$$

which is identical to that for the mosaic crystal description given below.

For a polarized incident beam (as for synchrotron radiation), the factor $[1+\cos^2(2\theta)]/2$ in (14) will be replaced by unity if the electric vector is perpendicular to the plane of reflection and by $\cos^2(2\theta)$ if the electric vector is parallel to the plane of reflection.

As we have noted in an earlier report [18], the measured value of R is essentially unaffected by diffraction line broadening effects generally. If, however, the x-ray line source energy width is relatively large, R then represents an average value for this energy interval. (R is not a useful, well defined reflectivity parameter if a significant absorption edge of the multilayer falls within this energy level.)

For low energy x-ray analyzers, because of the higher absorption within the multilayer (hence fewer effective reflecting planes), the intrinsic diffraction line widths are relatively large. The measured line widths may be further broadened by a mosaic quality of the multilayer structure (discussed below), by the energy width of the radiation "line" source, and by instrumental collimation widths. Often these effects can be accurately "folded" into the Lorentzian distribution. If these additional broadening effects are themselves Lorentzian (e.g., as for many emission-line sources), the fold yields another Lorentzian with the widths linearly additive. If, however, an additional line broadening effect is more accurately described as Gaussian (e.g., typical instrumental broadening), the fold yields a Voigt distribution for which a simple but non-linear addition to the Lorentzian FWHM can usually be made to within a good approximation [19], and is presented in Sect. IV.

D. The Mosaic Multilayer Model

It is often helpful in our understanding of multilayer reflection to compare the result obtained for the integrated relectivity, R, from the <u>MDP</u> model for an ideally perfect crystal slab to that from the <u>Mosaic</u> model for a slab which is ideally imperfect. In the mosaic crystal model the slab is assumed to be broken up into a mosaic of small well-ordered "crystallite" regions which reflect coherently, but have a random phase relationship with the other reflecting segments of the multilayer. Conventionally, the mosaic quality is considered to arise from crystallites of small lateral dimensions and thicknesses with their reflecting planes slightly and randomly

deviating from being parallel to the multilayer surface. A diffraction line broadening results from the random orientation as well as from the small number of contributing reflecting planes within the thin crystallites. Another expected mosaic quality likely for large spacing, "soft" multilayers is that of stacking within the slab of many independently and coherently scattering, essentially parallel thin layer systems because of random spacings between these regions and/or because of a region-to-region variation of the d-spacings (e.g., in some sputtered-or-evaporated multilayers). It is easy to establish the integrated intensity reflected from an independently coherent crystallite or thin layer region using a simple kinematical calculation (allowed because the absorption and multiple reflection effects are negligible for the small thicknesses involved. See James [12] beginning with his Eq. (2.2).) In the derivation of the integrated reflectivity, R_m, for the mosaic multilayer slab, the intensities (rather than amplitudes) are integrated through all angles and are summed from all regions of the slab taking into account the reduction of the intensity to and from each segment, $\exp(-2\mu z/\sin\theta)$. Here μ is the linear absorption coefficient and $2z/\sin\theta$ is the absorption path into and out from the differential segment at depth z within the multilayer slab (see Fig. 11). This integrated reflectivity, R_m, is easily shown to be:

$$R_m = \frac{r_o^2\lambda^3}{2\mu d^2}[(MF_1)^2 + (MF_2)^2]\frac{(1+\cos^2 2\theta)}{2\sin 2\theta} \tag{28}$$

Note: the mosaic model cannot predict diffraction line profiles, $I(\theta)$, which must depend upon the type and degree of the imperfections. Nevertheless, it predicts, for the low-energy x-ray region of interest here, essentially the <u>same</u> integrated reflectivity as that predicted by the MDP model. (See, for example, the results for W-C, Langmuir-Blodgett and Acid-Phthalate multilayers presented in [16].) As noted above, the Lorentzian approximation of the MDP distribution (neglecting multiple reflection contributions) and the Mosaic model yield identical analytical results for the integrated reflectivity, R.

E. Determination and Parameterization of MF for Multilayer Systems

The analytical model equations presented above require for a given photon energy or wavelength only the d-spacing and the unit area structure factor, MF, for their evaluation. General expressions for MF have been given in (14) and (15). We now present specific examples of the MF functions with appropriate parameterization which may then be applied to yield efficient,

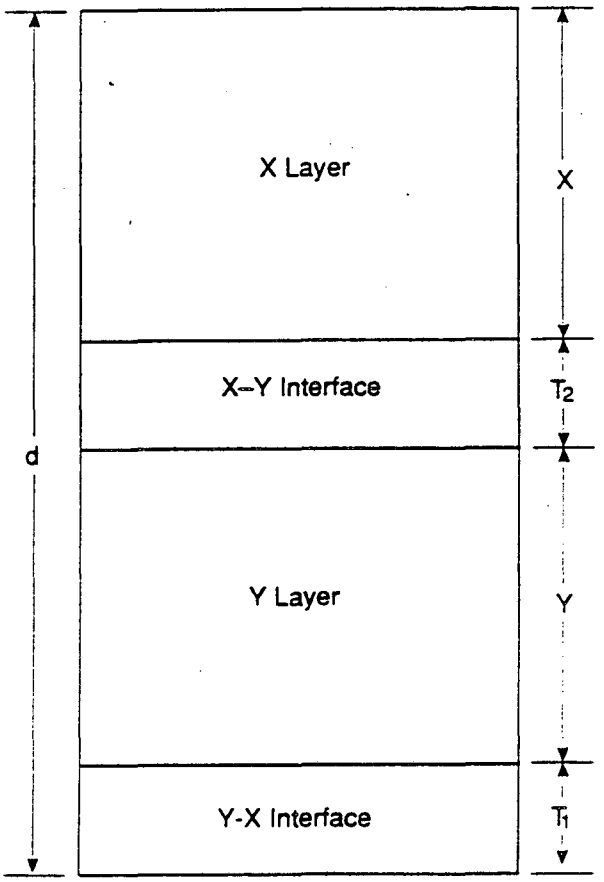

XBL 894-6211

12. Defining the geometry of the sputtered-or-evaporated multilayer's periodic layered structure (cell) of total thickness, d. X and Y are the thicknesses of the pure "light" and "heavy" layers respectively. T_1 and T_2 are the thicknesses of possible interface transition regions.

analytical, semi-empirical characterizations of practical multilayers.

Inside the multilayer, as a result of <u>refraction</u>, the angle of incidence and the wavelength at a unit cell plane must be the refraction modified values, θ' and λ'. The angle after refraction, θ', and the modified wavelength, λ', which must be used in the description of the wave interference within the multilayer, are given by Snell's Law, $\cos\theta/\cos\theta' = 1-\delta = \lambda/\lambda'$. We use here only the real part of the refractive index, $1-\delta$, because it can be easily shown that for x-ray refraction effects the first order terms in β cancel. In our model description of multilayers in the low energy x-ray region where refraction effects become relatively large, we replace the ratio, $\sin\theta/\lambda$ which appears in the structure factor F, by $\sin\theta'/\lambda'$ (in the parameter, $\phi = 4\pi\sin\theta/\lambda$ appearing in (14) and (15) above). In terms of δ, we may easily obtain from Snell's law the relation:

$$\frac{\sin\theta'}{\lambda'} = \frac{\sin\theta}{\lambda}\sqrt{1-\frac{2\delta-\delta^2}{\sin^2\theta}} \tag{29}$$

where δ is given by (14) and (22) as $r_o\lambda^2 MF_1(0)/2\pi d$.

(1) MF for Natural Crystal Multilayers

The unit cell structure for most natural crystals that can be effectively applied as long wavelength multilayer analyzers (e.g., mica and the acid phthalates) have a symmetry plane from which we can describe the one-dimensional distribution of atoms. Setting z=0 at the symmetry plane reduces the summation involving the sine terms in (14), to zero value.

The determination of MF by (14) requires the following parameters: the d-spacing along the coordinate, z, perpendicular to the multilayer surface; the unit cell cross section area, α, (in a plane perpendicular to z); and the number, species and z-coordinates of the atoms within the unit cell.

In Appendix E we outline the procedure for determining the one-dimensional multilayer structure (values of n_q, z_q) from the three-dimensional crystallographic structure. Also in Appendix E we present our calculations for the two natural crystal multilayers, mica (clear muscovite) and potassium acid phthalate (KAP), of the number and z-coordinates of the atoms within their unit cells and of their associated d-spacing and cross-sectional area, α. In Appendix F we present these data for the synthesized Langmuir-Blodgett "crystal" multilayer, lead stearate. (Also in Appendix F is outlined our procedures for constructing the LB multilayers and determining their structure.)

2. MF for Sputtered-or-Evaporated Multilayers

We assume that with the dense atomic packing of the sputtered or evaporated multilayers and with the relatively large Fresnel zone areas involved that permit the use of average atomic density values (even with appreciable statistical "roughness") we can accurately apply the continuous distribution integral (15) to calculate MF for these multilayers.

Note: For the sputtered or evaporated x-ray multilayer analyzers, the contribution to the reflected amplitude generated by multiple reflections within the multilayer will usually be small compared to that reflected directly to the detector. Therefore the area of the effective Fresnel zones involved is approximately that of the first elliptical zone (see Fig. 4) and equal to $\pi r\lambda/\sin\theta$ from (7) where r is the distance to the detector. For angles corresponding to a first order reflection ($\sin\theta = \lambda/2d$) this effective Fresnel zone area becomes simply $2\pi rd$. For example, with an analyzer-to-detector distance of 15 cm and a d-spacing of 100 Å, the Fresnel zone area is about 10,000 square microns. Hence fluctuations in the density of a reflecting plane of dimensions less than one micron may be described as statistically smooth and definable by a mean density value. However, for multiple reflections between layers, r for

the distance to the next layer is $d/\sin\theta$ and therefore in this case becomes about 150 Å. The effective Fresnel zone areas then become 10^7 times smaller, so that fluctuations must be within 10 $Å^2$ for the same smoothness statistics. Therefore, interface roughness would be expected to greatly reduce coherence for multiple reflections within sputtered multilayers. We would thus expect the Lorentzian approximation to the MDP model given in (23) to be an accurate one.

To set up the integral (15) we define a generalized multilayer geometry with the pure "light" and "heavy" layer thicknesses equal to X and Y, and with possible transition region thicknesses, T_1 and T_2 as shown in Fig. 12 for this unit cell.

In Appendix G, we present a brief description of the deposition processes that are typically applied for the construction of multilayer analyzers. The nature of the transition regions at the interfaces between the light and heavy layers will depend upon the materials involved and upon the conditions of the deposition process. We list below the relations obtained by integrating (15) to yield MF functions for four basic types of interface structure.

(a) Sharp Interface ($T_1 = T_2 = 0$)

$$MF = \frac{1}{i\phi'}\left[n_{xo}f_x(e^{i\phi' d} - e^{i\phi' Y}) + n_{yo}f_y(e^{i\phi' Y} - 1)\right] \tag{30}$$

n_{xo}, f_x and n_{yo}, f_y are the <u>atomic densities</u> and the complex atomic scattering factors for the light (x) and heavy (y) layers respectively, and $\phi' = 4\pi\sin\theta'/\lambda'$.

(b) Compound Interface ($T_1 = T_2 = T$)

For a uniform, compound material interface region characterized by n_{zo}, f_{zo} (e.g., a possible tungsten carbide region between sputtered W and C.)

$$MF = \frac{1}{i\phi'}\left[n_{xo}f_x(e^{i\phi' d} - e^{i\phi'(Y+2T)}) + n_{yo}f_y(e^{i\phi' Y} - 1)e^{i\phi' T} + n_{zo}f_z(e^{i\phi' T} - 1)(e^{i\phi'(Y+T)} + 1)\right] \tag{31}$$

(c) Symmetrical Linear Transition Interface ($T_1 = T_2 = T$)

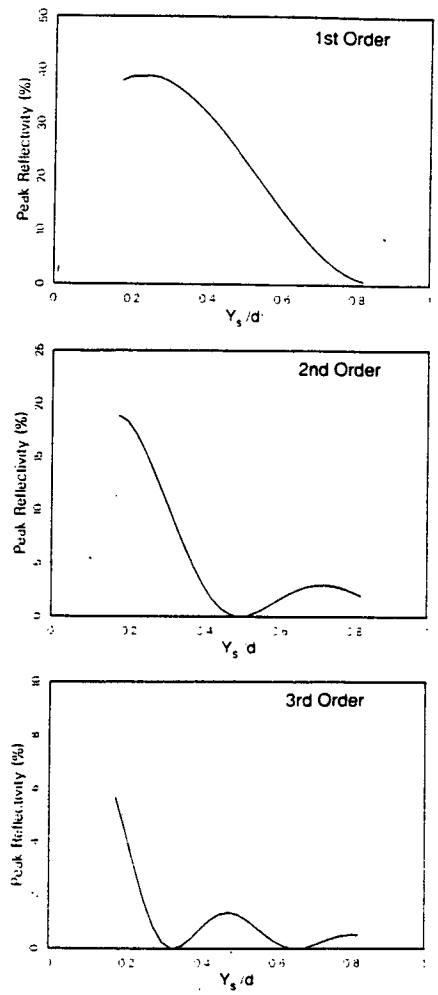

13. The dependence given by $|B|^2$ (Equ. (38)) of the peak reflectivity upon Y_s/d for the first three Bragg diffraction orders. (Y_s/d measures the volume fraction of the "heavy" constituent and is equal to $(Y+(T_1+T_2)/2)/d$ for the linear transition model.) These values for P are normalized for the reflection of 13.3 Å/930 eV radiation from a C-W multilayer of 50 Å d-spacing, N = 100 and with a linear transition layer thickness, $T_1=T_2=T=8$ Å. Illustrated here are the predicted high-order diffraction suppression values for Y_s/d and the general decrease in peak intensities as absorption increases with the higher values of Y_s/d. Y_s/d is simply determined by the relative sputtering deposition times set for the heavy and light constituents.

As suggested above we may define a continuous function, $n_q(z)$ for an interface distribution of the x and y elements resulting, for example, from implantation or diffusion and/or from roughness providing that the fluctuations within the differential layers are of less than micron dimensions. We consider here density functions within the transition layer that decrease and increase with z linearly in the mixing of the two elements. We also make the simplifying assumption that the volumes occupied by the x and y element are the same throughout the layer pair and equal to $(n_{xo})^{-1}$ and $(n_{yo})^{-1}$ respectively.

$$MF = \frac{1}{i\phi'}\left\{n_{xo}f_x(e^{i\phi' d}-1)+(n_{yo}f_y-n_{xo}f_x)\left[\frac{1}{i\phi' T}(e^{i\phi' T}-1)(1-e^{i\phi'(Y+T)})\right]\right\} \tag{32}$$

(d) Asymmetrical Linear Transition Interface ($T_1 \neq T_2$)

This case describes, for example, the possibility of implanting the heavy element more deeply into the light layer and than for sputtering the light element into the heavy layer.

$$MF = \frac{1}{i\phi'}\left\{n_{xo}f_x(e^{i\phi' d}-1)+(n_{yo}f_y-n_{xo}f_x)\left[\frac{1}{i\phi' T_1}(e^{i\phi' T_1}-1)-\frac{1}{i\phi' T_2}(e^{i\phi' T_2}-1)e^{i\phi'(Y+T_1)}\right]\right\} \tag{33}$$

F. Predicted Effects of MF-Parameters upon Multilayer Reflectivity

For the sub-kilovolt region it was noted above that the MDP multilayer model reduces to a Lorentzian described by (23) through (27) yielding the following dependence upon MF (= MF_1+iMF_2):

$$\begin{aligned} R &\sim [(MF_1)^2+(MF_2)^2]/MF_2(0) \\ P &\sim [(MF_1)^2+(MF_2)^2]/(MF_2(0))^2 \\ \omega &\sim F_2(0) \end{aligned} \tag{34}$$

where F(0), as noted earlier, may be related to the linear absorption coefficient, μ, and to the optical constants, δ and β, by the relations:

$$\begin{aligned} \delta &= \frac{r_o\lambda^2}{2\pi d}MF_1(0) \\ \beta &= \frac{r_o\lambda^2}{2\pi d}F_2(0) = \frac{\mu\lambda}{4\pi} \end{aligned} \tag{35}$$

In our modeling of practical multilayers for this study we have chosen to apply only the first two terms of a series expansion for the atomic density functions within the transition layers, [n(z) = a+bz] as described above for the <u>Linear Transition Model</u>. We now rewrite (32) in order to identify more specifically the dependence of this MF upon its material and structural parameters. We are interested only in MF around the Bragg diffraction angles and therefore have re-expressed the phase factor (ϕ') in (32), using the Bragg Equation, $m\lambda' = 2d\sin\theta'$:

$\phi' = 4\pi\sin\theta'/\lambda' = 2\pi m/d$

and setting the exp(i2πm) term equal to unity. MF in (32) near the Bragg angles becomes:

$$MF = \frac{d(n_{xo}f_x - n_{yo}f_y)}{2\pi m}\left[1 - e^{i2\pi m(Y+T)/d}\right]\left[\frac{d}{2\pi mT}(e^{i2\pi mT/d} - 1)\right] = A \cdot B \cdot C \tag{36}$$

Because, as noted above, the multilayer's integrated and peak reflectivities, R and P, are proportional to $(MF_1)^2 + (MF_2)^2$, we multiply A, B and C in (36) by their respective complex conjugates to obtain:

$$|MF|^2 = (MF_1)^2 + (MF_2)^2 = |A|^2\ |B|^2\ |C|^2$$

where $|A|^2$, $|B|^2$ and $|C|^2$ are given by:

$$|A|^2 = \left(\frac{d}{2\pi m}\right)^2 \left[(n_{xo}f_{1x} - n_{yo}f_{1y})^2 + (n_{xo}f_{2x} - n_{yo}f_{2y})^2\right] \tag{37}$$

$$|B|^2 = 2\left[1 - \cos\left(2\pi m\frac{Y+T}{d}\right)\right] \tag{38}$$

$$|C|^2 = 2\left(\frac{d}{2\pi mT}\right)^2 \left[1 - \cos\left(2\pi m\frac{T}{d}\right)\right] \tag{39}$$

$|A|^2$ expresses the effect of composition of the multilayer through the difference or "contrast" between the scattering factor per unit volume of the "heavy" and light" elements of the layer-pair.

$|B|^2$ expresses the effect of the fractional amount of the unit cell layer that is originally deposited with the "heavy " element, Y_s/d, which is equal to (Y+T)/d for this linear transition model. This parameter is simply preset by the relative sputtering times given the two elements.

$|C|^2$ expresses the effect of the relative size of the transition region thickness, T/d, which, for a given choice of heavy and light materials, may often be controlled by sputtering conditions.

(a) Suppression of Higher diffraction Orders for $T_1 = T_2$

An important design requirement is often that a particular high order background reflection be suppressed (usually the second

order radiation). This may be fulfilled, by adjusting the heavy element thickness fraction, Y_s/d, so that B in MF is equal to zero. We note from (36) that the zero values for $|B|^2$ occur for:

$$(Y+T)/d = Y_s/d = n/m \tag{40}$$

for n equal to any positive integer less than m. For example second order suppression will occur for $Y_s/d = 1/2$ which is achieved by sputtering equal volume amounts of the heavy and light elements.

Missing orders may also occur when $|C|^2$ has its zero values. It may readily be shown, using (39), that this will occur for:

$$T/d = n/m \tag{41}$$

for n equal to any positive integer equal to or less than m/2.

In our semi-empirical modeling of practical multilayers by fitting experimental spectra through several diffraction orders (discussed below) we have often been able to immediately verify values for Y_s (and sometimes for T) by noting which orders are strongly suppressed.

(b) Suppression of Higher Diffraction Orders for $T_1 \neq T_2$

Following the procedure presented above, we may also describe the effect of the thickness parameters upon MF for the asymmetrical linear transition multilayer model. For example, it may be shown that for this type of multilayer, MF as given in (33) will have its zero values and m^{th} diffraction order suppression when:

$$T_1/d = l/m \quad \text{and} \quad T_2/d = n/m \tag{42}$$

for positive integer values of ℓ and n, and for $\ell + n \leq m$.

(c) Summarizing the Effects of Sputtered-or-Evaporated Multilayer Structure upon Reflectivity

In Sect. II we introduced a "Figure of Merit" for the multilayer analyzer that is the product of its resolving power

$\lambda/\Delta\lambda$, and the "signal" within the diffraction line, which is dependent upon the multilayer's material properties through the factor R/μ. It follows from the Lorentzian description of a diffraction line profile as given in Eqs. (25) and (26) that the peak intensity, P, is also proportional to R/μ and is therefore a measure of this Figure of Merit.

In Figs. 13, 14 and 15 we plot the peak reflectivity, P, of a hypothetical multilayer of C-W of 50 Å d-spacing, N = 100 layer-pairs, for the first three diffraction orders as a function of the structural parameters introduced above.

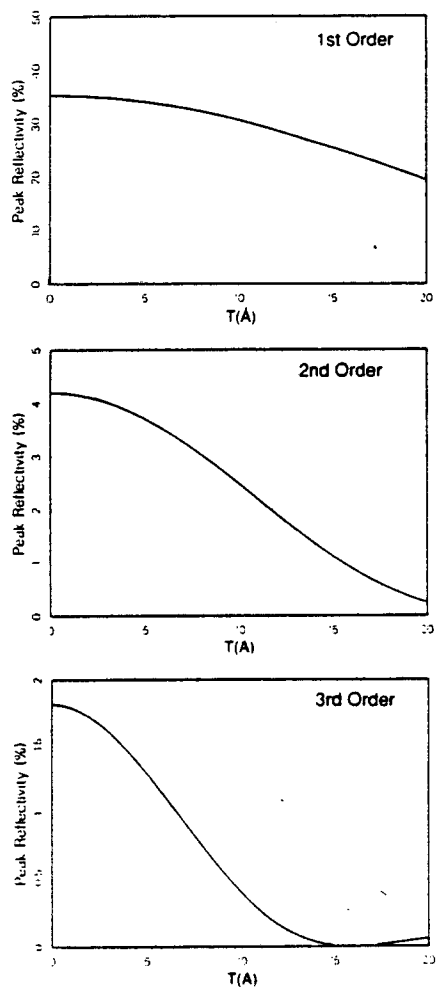

14. The dependence given by $|C|^2$ (Equ. (39)) of peak reflectivity upon the transition layer thickness, T (using the linear transition model with $T_1=T_2=T$). These normalized values of P are for the reflection of 13.3 Å/930 eV radiation from a 50 Å d-spacing multilayer of C-W, N = 100 and with Y_s/d set to 0.4. Illustrated here is the predicted third-order diffraction suppression at T = d/3 = 17 Å and also indicated is the marked decrease generally of peak intensities with increasing T.

15. Effect of the asymmetry factor, T_1/T_2, upon the relationship between the peak reflectivity and the average transition layer thickness, $T_{ave} = (T_1+T_2)/2$. These plots of P vs T_{ave} have been obtained using MF given in (33) for the reflection of 13.3 Å/930 eV radiation from a C-W multilayer of 50 Å d-spacing, N = 100 and $Y_s/d = 0.4$. As expected, asymmetry "softens" the effect of order suppression and of a general decrease in peak reflectivity from that shown here and in Fig. 14 for $T_1 = T_2$.

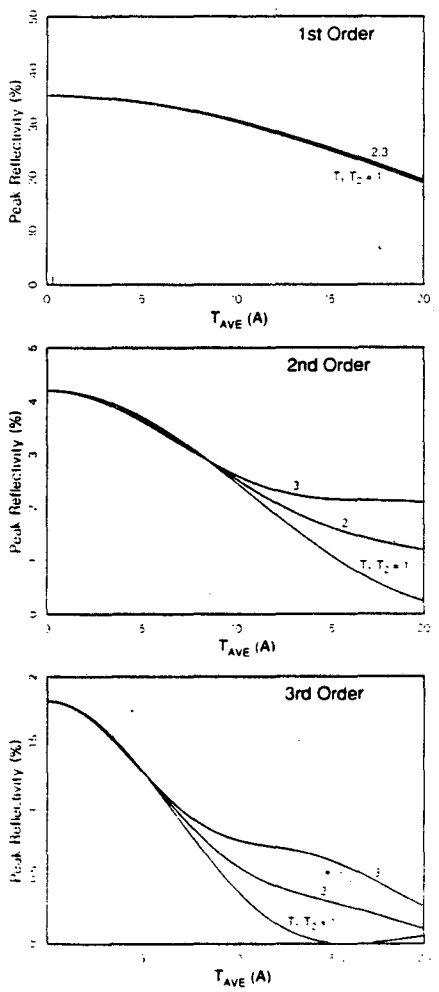

Figure 15

In Fig. 13 is plotted P vs Y_s/d for the linear transition multilayer ($T_1=T_2=T=8Å$). Indicated here along with the zero-values predicted above is the general decrease in the peak reflectivities with increasing Y_s/d (causing increased $F_2(0)$ and therefore absorption within the multilayer.)

In Fig. 14 is plotted P vs T with Y_s/d fixed at 0.4 for the linear transition multilayer ($T_1=T_2=T$). Note the suppression of the third order at T = 17 Å corresponding to d/3 as predicted by (41). Also illustrated here is the fact that increasing the transition region thickness rapidly decreases peak reflectivities generally.

In Fig. 15 is plotted P vs T_{ave} [$T_{ave} = (T_1+T_2)/2$] for different values of the <u>asymmetry factor</u>, equal to T_1/T_2. As expected, increasing asymmetry "softens" the effect of order suppression and of the decrease of reflectivity as T_{ave} increases.

In the next Section we describe the experimental procedures that have been developed in this laboratory for the measurement of the multilayer reflectivity characteristics including $I(\theta)$, R, ω and P. These experimental data are needed to validate the application of the detailed model descriptions which have been given here for absolute spectrometry.

IV. MEASUREMENT OF MULTILAYER REFLECTIVITY

The detailed characteristics of multilayer reflectivity e.g. as depicted in Fig. 2, have been measured using a specially designed vacuum spectrograph that is schematically described in Fig. 16. A fine slit and filter is positioned at the isolation gate window of one of our demountable x-ray tubes [19] to provide a strong, characteristic line source in the 50-10,000 eV region. The multilayer is mounted with its surface on the axis of a precision θ - 2θ goniometer. A sharply defined incident beam is restricted to a small sampled area (typically a few millimeters) of the multilayer by a razor blade edge placed close to its surface. The angular resolution of the measurement is set by the divergence of the incident beam which is essentially established by the slit width at the x-ray source which is 120 cm from the goniometer axis. This is usually set to an angular resolution width that is small as compared to the diffraction line width, ω, of the multilayer analyzer. The reflected beam is measured by a sub-atmospheric, gas flow proportional counter ("tuned" in pressure to about 90% gas path absorption for the wavelength being measured) with a window 10 cm from the goniometer axis which accepts a beam width of a few millimeters off the multilayer analyzer and with a slit width that is larger than that of the reflected beam. This effective incident beam is

limited in vertical width by the projection of the opening at the razor edge and is therefore angle-dependent and proportional to $\cos\theta$ as noted in Fig. 16.

In the small angle region an inflection point appears in the reflected intensity at $\theta = 0$, as illustrated in Fig. 17. It may be readily shown that the intensity at this feature is $I_o/2$ so that both the incident intensity, I_o, and the zero angle calibration of the spectrograph are determined in this way.

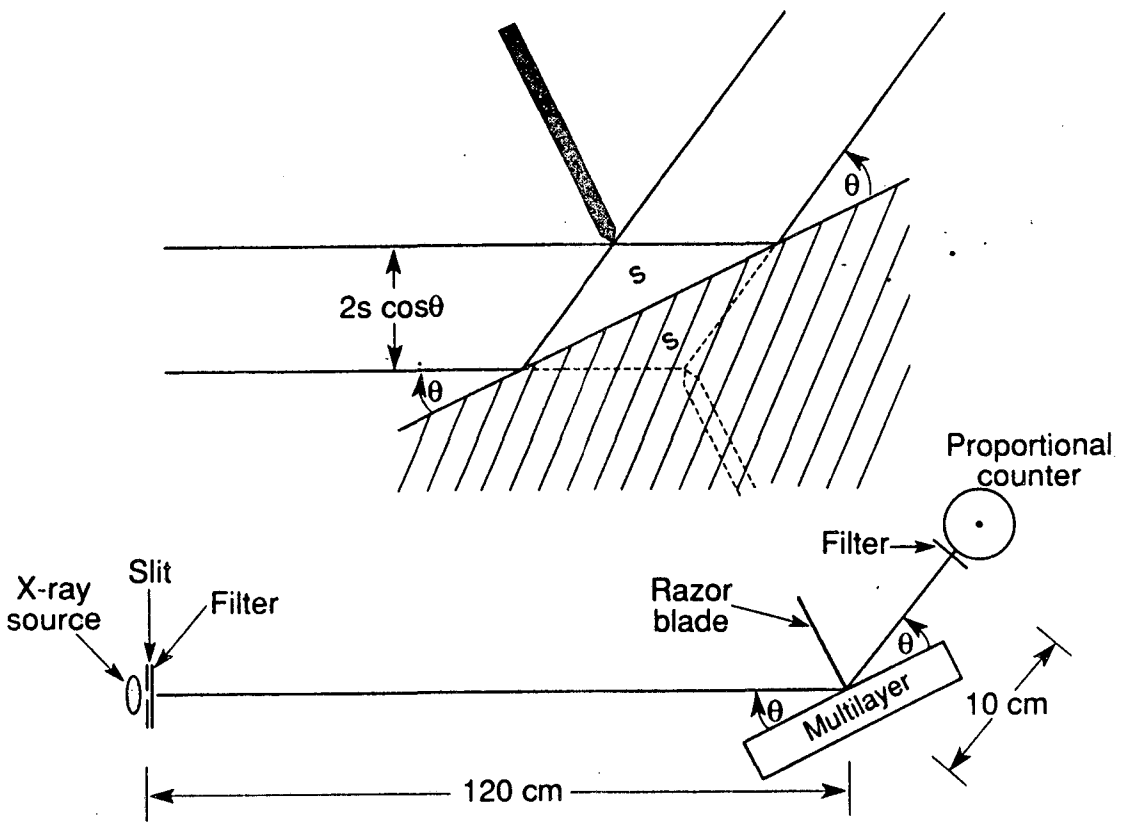

16. The geometry of the specially designed spectrograph for the absolute experimental characterization of multilayers. A fine slit and filter is placed at the vacuum isolation gate of a high-power, broad focal spot, demountable x-ray tube. The multilayer surface is mounted on the axis of a precision θ-2θ goniometer which is 120 cm from the source slit. A razor edge is mounted on the crystal holder and is located at a small distance, s, above the multilayer and goniometer axis to establish a collimated ray system from the source that "samples" a few millimeters of multilayer surface and is of a net divergence that is small compared to the angular width of the diffraction line being measured. A "pressure-tuned" gas flow proportional counter is mounted on the 2θ-arm with its window 10 cm from the goniometer axis. The counter window accepts the total reflected beam which is limited only by the slits at the source and multilayer. A strong characteristic line from the low kilovoltage source is isolated from associated lower-and-higher energy background radiation by the source and counter filter-windows and by the pulse-height-discrimination "window" of the pressure-tuned proportional counter. As a spectrum is scanned, usually through several diffraction orders, it is displayed on a multi-channel analyzer which is programmed to present the θ_n, E_n, w_n and P_n values for each diffraction line. The measured spectra are similar to that depicted in Fig. 2. Increasing, normalized steps in source intensity are applied in order to maintain uniformly good statistics for the higher order diffraction lines.

XBL 894-6210

17. Using the measured characteristic onset of the low-angle "total reflection" to determine the incident intensity, I_0, at the multilayer and the zero-angle position of the spectrograph. Shown here are predicted onset responses for several levels (%) of low-angle specular reflectivity along with a typical measured onset characteristic. The inflection point at $\theta = 0$ and $I = AI_0$ is at a relative angle of s/a from the initial zero-intensity point. (A is the slit-defined cross sectional area beneath the razor edge and AI_0 is the no. of photons per sec directly reaching the detector at $\theta=0$.) The incident no. of photons/sec that may be reflected from the multilayer at angles beyond the onset region is $2I_0A\cos\theta$.

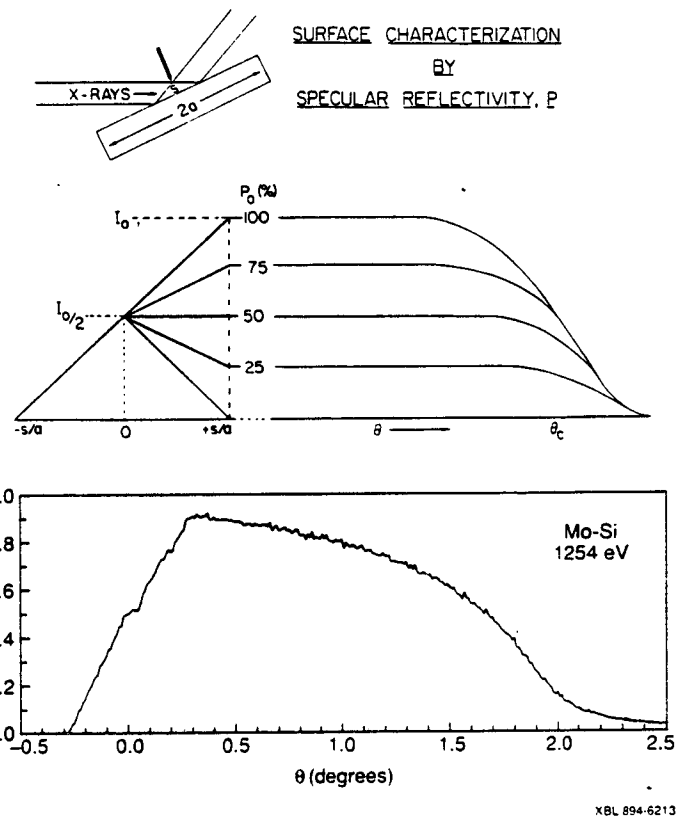

The intrinsic full-width-at-half-maximum (FWHM) of the diffraction line profile (in θ) may be simply determined in terms of the experimentally measured width, ω_x, the Gaussian instrumental width, g, and the Lorentzian emission source line energy width, ϵ, by the following expression [19]:

$$\omega = \omega_x[1 - (g/\omega_x)^2] - \epsilon \tag{43}$$

where ϵ is given by (3):

$$\epsilon = \frac{e}{E}\tan\theta \tag{44}$$

for which the x-ray source line of photon energy, E, has an effective energy width of e.

The integrated reflectivity is determined by the total number of photons reflected, N_x, as the diffraction line is scanned at an angular rate in θ of $d\theta/dt$ by the relation[18]:

$$R = \frac{N_x}{I_o \cos\theta}\left(\frac{d\theta}{dt}\right) \tag{45}$$

The experimental peak reflectivity, P_x, is measured as the ratio of the number of photons reflected at the peak of the diffraction profile to that of the incident beam intensity, $I_o \cos\theta$. Assuming that the shape of the intrinsic diffraction profile is essentially the same as that for the experimentally measured profile, the area under the profile, R, (integrated reflectivity) is equal to $K\omega P$ and also to $K\omega_x P_x$, where K is a shape factor [see (25) for example]. We may therefore obtain an estimate of the intrinsic peak reflectivity, P, by the relation:

$$P = \frac{\omega_x}{\omega} P_x \tag{46}$$

Note: It is required that the I_o value used in these measurements be for only those incident photons of energy that is within the characteristic line source that is being measured. Low energy background photons can usually be suppressed by an appropriate filter. The high energy photon background is effectively eliminated by the pulse height discrimination of the "tuned" proportional counter. For our measurements, the Fresnel-reflection region and several orders of diffraction lines are measured (at appropriate, normalized x-ray intensities), recorded, and displayed with a multi-channel analyzer (MCA). This spectrum along with the associated extended pulse height spectrum for the detector provide an accurate check on the existence of any significant background radiation that may need to be further eliminated literally or by correction.

The MCA and an associated laboratory computer are programmed to permit an immediate determination for each diffraction line of its centroid position, θ_x, FWHM, ω_x, peak reflectivity, P_x, and integrated reflectivity, R. These values are derived from a diffraction line profile that is generated for the region $+3\omega$ and -3ω from the peak position <u>after</u> a background subtraction is made for approximately this region. This background subtraction is usually a small correction because only those diffraction lines are measured which are at angles greater than $3\theta_c$ as has been discussed in Sect. III for our corresponding model definitions of R, ω and P.

These data and the spectra are transferred from the MCA to the small desktop computer and processed for the final semi-empirical characterization of a multilayer. Examples of the semi-empirical characterizations are presented in the next sections.

V. SEMI-EMPIRICAL MODELING FOR MULTILAYER CHARACTERIZATION

In our testing of the validity and applicability of the model descriptions that have been presented in Sect. III, we compare theory and experiment principally for the integrated reflectivity parameter, R, which is the basic parameter that is applied in most quantitative x-ray spectral analyses. Unlike the line shape parameters, i.e., the FWHM and the relative peak intensity, P(%), the measured R values are essentially unaffected by the spectrographic resolution (the instrumental resolution and the energy width of the incident "line" source). For the low energy region of interest here (50-1000 eV), the theoretical predictions of the integrated reflectivity, R, do not require knowledge of the degree and type of imperfections of the analyzer. (As noted in Sect. III, the dynamical, kinematical and mosaic models yield nearly the same values for R in this low energy region. For the practical multilayer analyzer R is accurately determined simply by the two quantities, MF and d.)

A. Determination of the Absolute d-Spacing

The absolute d-spacing, from the Bragg equation, is given by $m\lambda'/(2\sin\theta')$ where λ' and θ' are the values inside the multilayer. We define the measurable, effective spacing, d_x, by $m\lambda/(2\sin\theta)$. Using (29) we relate d to d_x values by:

$$d \simeq d_x(1 - \frac{\delta}{\sin^2\theta}) \tag{47}$$

where δ determines the multilayer's parameter, $MF_1(0)$, as given by (35). Because δ is very small compared to unity, we are able to determine d semi-empirically as the zero-angle, extrapolated limit of a d_x vs $\mathrm{cosec}^2\theta$ plot of d_x-θ data for several diffraction orders at a given photon energy. The slope of this linear plot yields a consistency check value for δ and $MF_1(0)$ at this photon energy (to be compared to these values as determined by using our tabulated atomic scattering factor data and semi-empirically determined MF values). An example of such determinations is presented in Fig. 18.[21]

B. Fitting MF for Natural Crystal and Langmuir-Blodgett Multilayer Characterization

For multilayers such as the natural crystals: mica and the acid phthalates, and the synthetic, Langmuir-Blodgett "crystals", MF values may often be determined simply by using (17) with

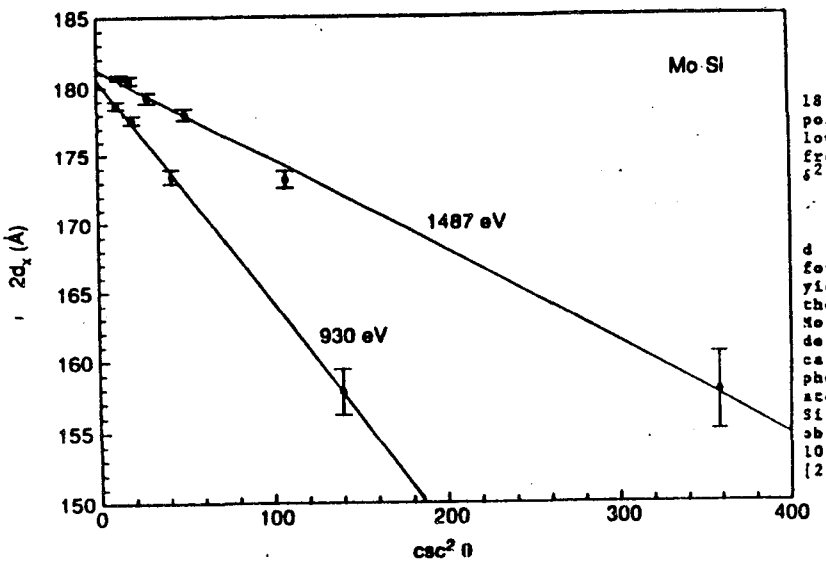

XBL 894-6714

18. The determination of absolute d-spacing from the angular positions of several diffraction orders for a given low-energy characteristic source line. It follows directly from Snell's law that after dropping the very small terms in δ^2 and β^2 we obtain the relation:

$$d_x = m\lambda/2\sin\theta = d(1-\delta\csc^2(\theta))$$

d is determined by the extrapolation of d_x vs $\csc^2(\theta)$ data for the several diffraction orders. The slope of this plot yields a value for the average δ value for the multilayer at the given photon energy. Shown here is this analysis for a Mo-Si multilayer for which our modeling procedures have determined the Y_s/d value to be 0.36, corresponding to a calculated δ value of 9.7×10^{-4} and 3.8×10^{-4} for the two photon energies, 930 eV and 1487 eV (using our tabulated atomic scattering factor data for the constituents, Mo and Si). From the measured slopes of the plots shown here we obtain for the corresponding δ-values 9.0×10^{-4} and 3.7×10^{-4}, in good agreement with our MDP model values (see [21]).

available crystallographic structure data and atomic scattering factors. The accuracy is sufficient to yield, with the MDP modeling, R-values that are in satisfactory agreement with those measured. (When, however, accurate experimental R-values differ systematically from the directly predicted ones, inaccurate values for the unit cell areal density, M, may be suspected, and our analytical MDP function may then be least-squares fit to the R_x vs photon energy, E, curves to determine semi-empirically a value for M. Because, as noted in (34), R is essentially proportional to M, we have often simply normalized (by raising or lowering) the model log R vs log E curves to fit the calibrating data for a particular crystal analyzer (assuming that the theoretically predicted relative energy dependence is precise and insensitive to small variations in its parameterization for atomic densities and scattering factors.) Detailed characterizations for mica, KAP and Lead Stearate multilayers based upon the crystallographic data in Appendices E and F and upon our atomic scattering factor tables [17] are presented in Sect. VI.

C. Fitting MF for Sputtered Multilayer Characterization

MF values for the sputtered or evaporated multilayers must always be determined semi-empirically because the unit cell structure is not "locked in" as for the crystal or molecular

multilayers. The relative amount of the heavy element initially deposited, Y_s/d, is usually difficult to precisely measure directly, as is the transition layer structure. For a given multilayer, we attempt to make these determinations by fitting the general MF expression (33) for the asymmetrical linear transition interfaces by varying the transition layer thicknesses, T_1 and T_2, and the pure heavy and light layer thicknesses, Y and X. Our fitting procedure is as follows: We apply our analytical MDP computer program [based upon (19) as described earlier] which predicts for a given MF and energy, E, the R-value as obtained by a numerical integration of $I(\epsilon)$ in the range $\pm 3\omega$ from the diffraction line <u>after</u> a background subtraction (similarly defined for the experimental R-value as discussed in Sect. IV). Assuming bulk densities for n_{xo} and n_{yo}, R(MDP) values are least-squares fit to a measured set of R(exp) values for appropriate energies and diffraction orders, varying Y, T_1 and T_2. Using these results to determine Y_s and an asymmetry ratio, T_1/T_2, we then repeat this fitting procedure varying now the density values and the transition layer thicknesses for our semi-empirically determined "best" values for n_{xo}, n_{yo}, Y, T_1 and T_2. (The variation of the density values is limited to the range 70-100 % of bulk values.)

We have carried out this semi-empirical modeling procedure upon a series of sputtered multilayer types obtained from three laboratory sources [21]. Presented here are the semi-empirically determined MF parameters for a representative set of nine of these multilayers. In Table 1 are presented the structure parameters, Y, T_1 and T_2 [$X = d-(Y+T_1+T_2)$]. In Tables 2 and 3 are presented the experimental R-values for the diffraction orders and photon energies measured and compared to our predicted R values. The relative standard deviation between the measured and predicted R-values for all measured diffraction orders (with no statistical weighting) for each multilayer are also included in Table 1.

1. "Best fit" values of the linear transition MF parameters, Y, T_1, T_2, ρ_x and ρ_y for nine representative semi-empirically characterized sputtered multilayers. Also given here are the relative standard deviations, $(R_{expt} - R_{theory})/R_{expt}$ for all diffraction orders and energies measured (See Tables 2) for the "best fit" determinations of the parameters for a given multilayer.

crystal designation	2d(Å)	N	Y	T_1	T_2	ρ_x	ρ_y	err
SiMo197	196.6	30	20.84	19.27	9.48	2.26	10.06	.192
SiV148	148.2	60	19.48	26.31	9.63	2.15	5.80	.127
CV96	96.0	60	20.35	10.99	10.99	1.87	5.76	.077
CV95	94.6	60	22.34	6.88	6.88	1.55	5.18	.042
CV62	62.0	90	11.67	8.09	8.09	2.20	6.11	.132
CW137	136.6	90	9.12	16.15	16.15	2.16	19.3	.186
CW75	75.2	75	13.31	7.73	7.73	2.16	16.95	.189
BNV60	60.0	50	11.33	6.62	6.62	2.26	6.04	.094
B4CPd108	107.8	75	23.69	15.06	15.06	1.88	10.66	.200

Table 1

Si - Mo 2d = 196.6Å

E (eV)	order	R_{expt}	R_{theory}
183.4	2	0.105	0.111
929.7	2	0.403	0.355
929.7	3	0.017	0.013
929.7	4	0.033	0.026
1486.7	2	0.385	0.408
1486.7	3	0.014	0.016
1486.7	4	0.028	0.032

C - V 2d = 96.0Å

E (eV)	order	R_{expt}	R_{theory}
192.6	1	1.196	1.194
277.0	1	2.319	2.365
929.7	1	0.539	0.557
929.7	2	0.030	0.033
1486.7	1	0.694	0.666
1486.7	2	0.052	0.046

C - W 2d = 75.2Å

E (eV)	order	R_{expt}	R_{theory}
192.6	1	4.200	2.985
929.7	1	2.040	1.903
929.7	2	0.020	0.019
929.7	1	0.014	0.011
1486.7	1	1.258	1.478
1486.7	2	0.016	0.018
1486.7	3	0.010	0.011

BN - V 2d = 69.0Å

E (eV)	order	R_{expt}	R_{theory}
277.0	1	0.271	0.288
929.7	1	0.451	0.394
929.7	2	0.023	0.024
1486.7	1	0.519	0.487
1486.7	2	0.028	0.027

C - V 2d = 62.0Å

E (eV)	order	R_{expt}	R_{theory}
929.7	1	0.314	0.341
929.7	2	0.012	0.013
1486.7	1	0.480	0.427
1486.7	2	0.019	0.017

C - W 2d = 136.6Å

E (eV)	order	R_{expt}	R_{theory}
277.0	1	5.691	4.863
277.0	2	0.220	0.170
929.7	1	2.740	2.875
929.7	2	0.174	0.134
929.7	3	0.002	0.002
1486.7	1	1.847	2.182
1486.7	2	0.106	0.114

Si - V 2d = 148.2Å

E (eV)	order	R_{expt}	R_{theory}
277.0	1	0.448	0.442
929.7	2	0.015	0.014
929.7	3	0.006	0.007
929.7	4	0.004	0.004
1486.7	1	1.411	1.435
1486.7	2	0.019	0.020
1486.7	3	0.014	0.011

C - V 2d = 94.6Å

E (eV)	order	R_{expt}	R_{theory}
192.6	1	1.501	1.406
277.0	1	2.468	2.463
929.7	1	0.603	0.634
929.7	2	0.046	0.045
1486.7	1	0.741	0.749
1486.7	2	0.061	0.062

B_4C - PD 2d = 107.8Å

E (eV)	order	R_{expt}	R_{theory}
183.4	1	3.139	3.081
192.6	1	1.245	1.625
929.7	2	0.074	0.065
929.7	3	.0004	.0004
1486.7	1	1.034	0.924
1486.7	2	0.105	0.077
1486.7	3	.0006	.0006

2. The experimental and "best fit" theoretical values of the integrated reflectivites at various diffraction orders and photon energies for nine representative multilayers of this investigation.

Crystal Type	T_1(Å)	T_2(Å)
Si - Mo	10	20
Si - V	10	25
C - V	8	8
C - W	8	8
BN - V	7	7
B_4C - Pd	15	15

Table 3

3. Nominal values for selected multilayers of semi-empirically determined linear transition interface thicknesses, T_1 and T_2, that may be applied to predict the reflectivity of any of these multilayers with any d-spacings sufficiently large to provide non-zero thicknesses for X and Y.

We identify the multilayers with the formula, ab#, where a is the top (last deposited) layer and b the next of the layer pair, and # is the 2d-value. It is of interest to note that there is a systematic difference in the determined T_1 and T_2 values for the same multilayer type as constructed at different laboratories. This observation suggests that the T values may be minimized by control of the sputtering procedure.

VI. APPLICATION FOR ABSOLUTE SPECTROMETRY

A. Detailed Characterization of Selected Multilayers for the 50-1000 eV Region

We would like now to apply the semi-empirical modeling procedures outlined above to obtain in detail the absolute values for the reflectivity characteristics R, P, ω and $E/\Delta E$ for selected examples of multilayer analyzers that can be effectively applied for absolute spectrometry in the 50-1000 eV region.

Presented in Figs. 19 and 20 are the reflectivity characteristic plots for Mica and KAP using the structural data given in Appendix E, and similarly, the reflectivity plots are presented in Fig. 21 for Lead Stearate based upon its structural data given in Appendix F. Experimental points in Figs. 19, 20 and 21 are from [21, 22, and 23].

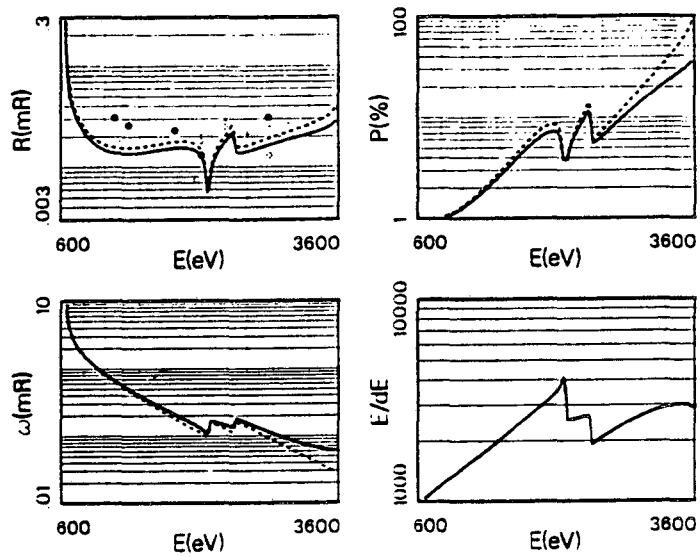

19. First-order reflectivity data, R, P, ω and E/ΔE, for Mica. (Calculated using our tabulated atomic scattering factors, the structure given in Appendix E and for Bragg reflections in the 10-80 deg range.) R(MDP) ___ and R(Mosaic) ---. Exp. data [22].

XBL 395-1692

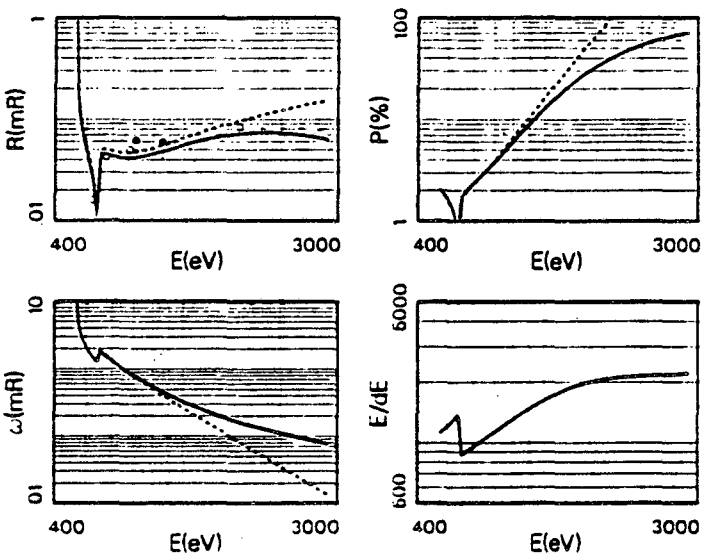

20. First-order reflectivity data, R, P, ω and E/ΔE, for Potassium Acid Phthalate (KAP). (Calculated using our tabulated atomic scattering factors, the structure given in Appendix E and for Bragg reflections in the 10-80 deg range.) R(MDP) ___ and R(Mosaic) ---. Exp. data [23].

XBL 395-1693

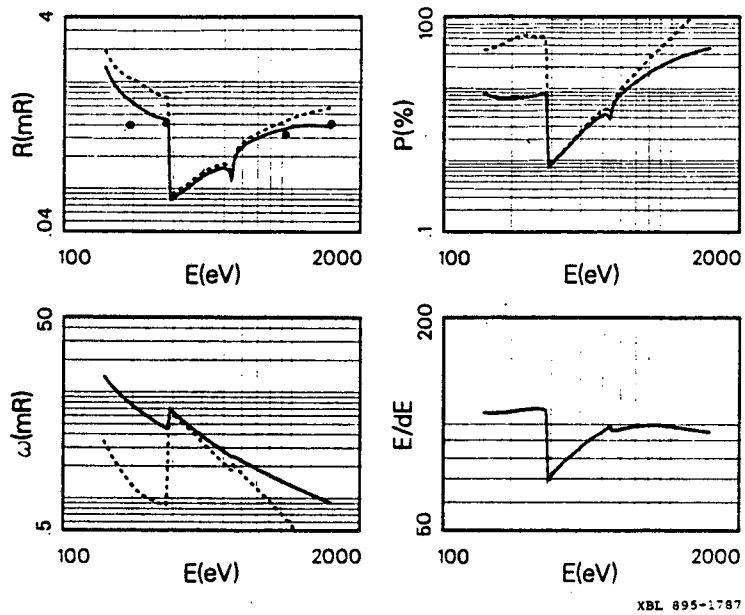

21. First-order reflectivity data, R, P, ω and E/ΔE, for lead stearate (PbSt). (Calculated using our tabulated atomic scattering factors, the structure given in Appendix F and for Bragg reflections in the 10-80 deg range.) Exp. data [24].

As has been discussed earlier, it is important when applying multilayer analyzers for absolute, optimized spectrometry to make measurements in the large-angle diffraction range. Consequently, our reflectivity plots are limited to the photon energies corresponding to first-order diffractions in the θ-range of 10° to 80° as fixed by the d-spacings of these multilayers.

An important advantage of the sputtered or evaporated multilayers is that the d-spacing can be "tailored" within a continuous range of values. Generally, as expressed in the MDP modeling, the optimum energy region of application for a given multilayer type is that for which the MF values are maximized--mostly through the energy dependence of the "contrast" factor, $|A|^2$ given in (37). The d-spacing may then be so chosen that it will place the first-order diffraction at the desired large angles for this optimum energy region. We shall assume here that for d-spacings which are large compared to the interface transition regions, the T_1 and T_2 values are determined principally by the sputtering materials and process and are <u>not</u> dependent upon the overall d-spacing. In Table 3 we list the semi-empirically determined nominal values of T_1 and T_2 for five

types of sputtered multilayers which we have selected as particularly promising. Using these parameters, we have plotted the R vs E curves for multilayers with 2d values of 50, 100 and 150 Å in order to identify the optimum energy regions for their application. These are presented in Figs. 22, 23 and 24.

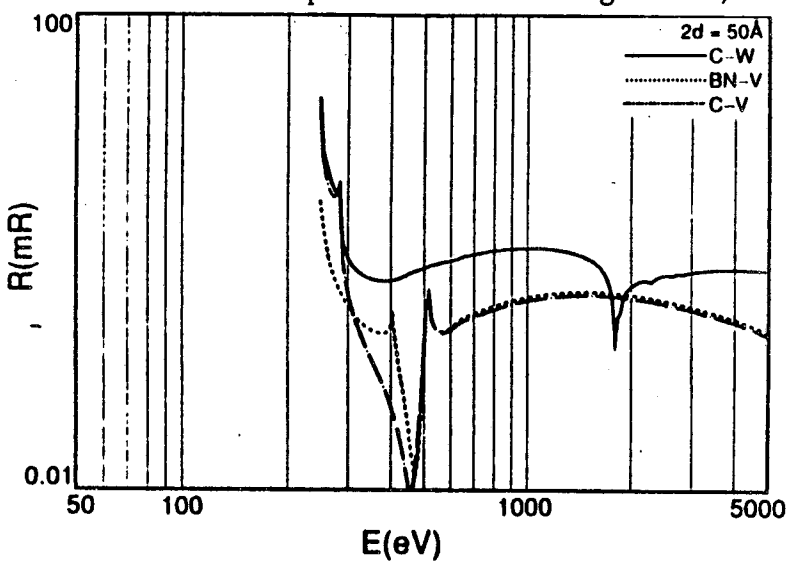

XBL 894-1609

22. Comparing the integrated reflectivities, R, for several practical sputtered multilayers with 2d = 50 Å that are appropriate for the shorter wavelength and hence for smaller d-spacing applications. The integrated reflectivity is calculated for N = 100 layer pairs, Y_s = 40 % and the transition layer thicknesses given in Table 3. C-W ___, BN-V -----, C-V -.-.- .

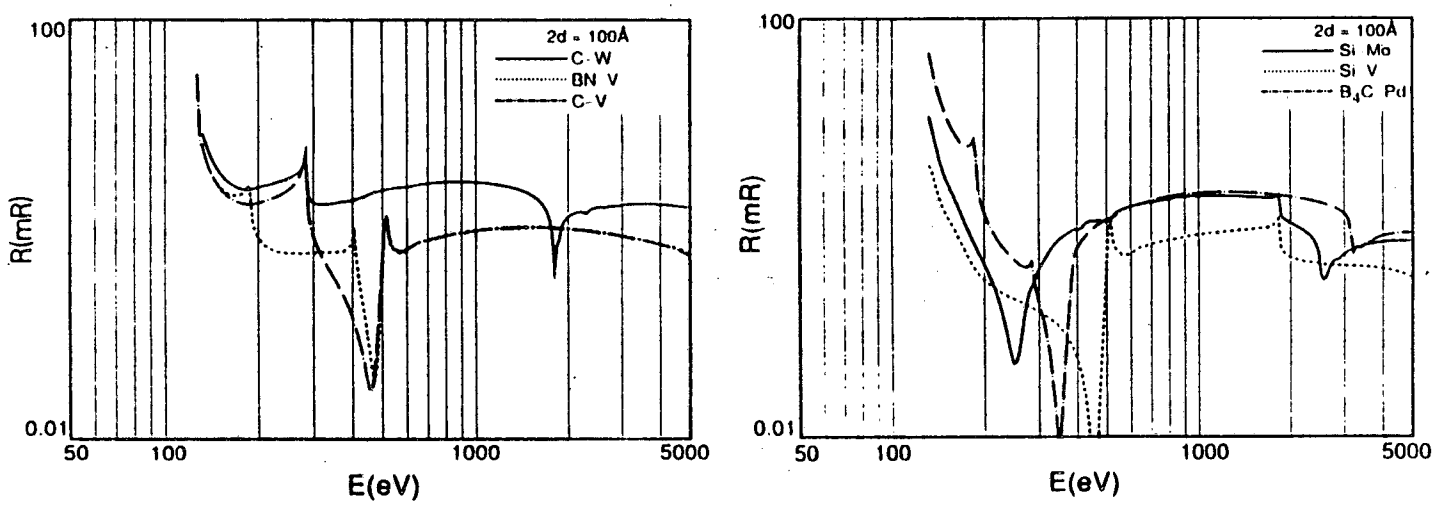

XBL 894-1605 XBL 894-1610

23. Comparing the integrated reflectivity, R, for practical sputtered multilayers with 2d = 100 Å. The integrated reflectivity is calculated for N = 100 layer pairs, Y_s = 40 % and the transition layer thicknesses given in Table 3. (a) C-W ___, BN-V ---, C-V -.-.-. (b) Si-Mo ___, Si-V ---, B_4C-Pd -.-.-.

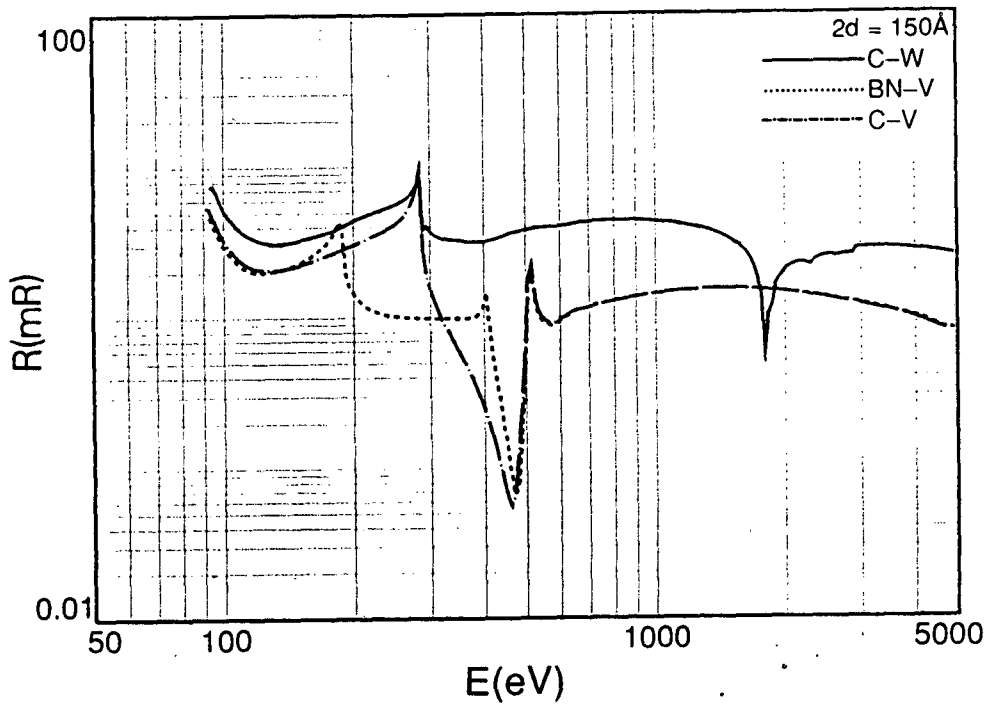

XBL 894-1608

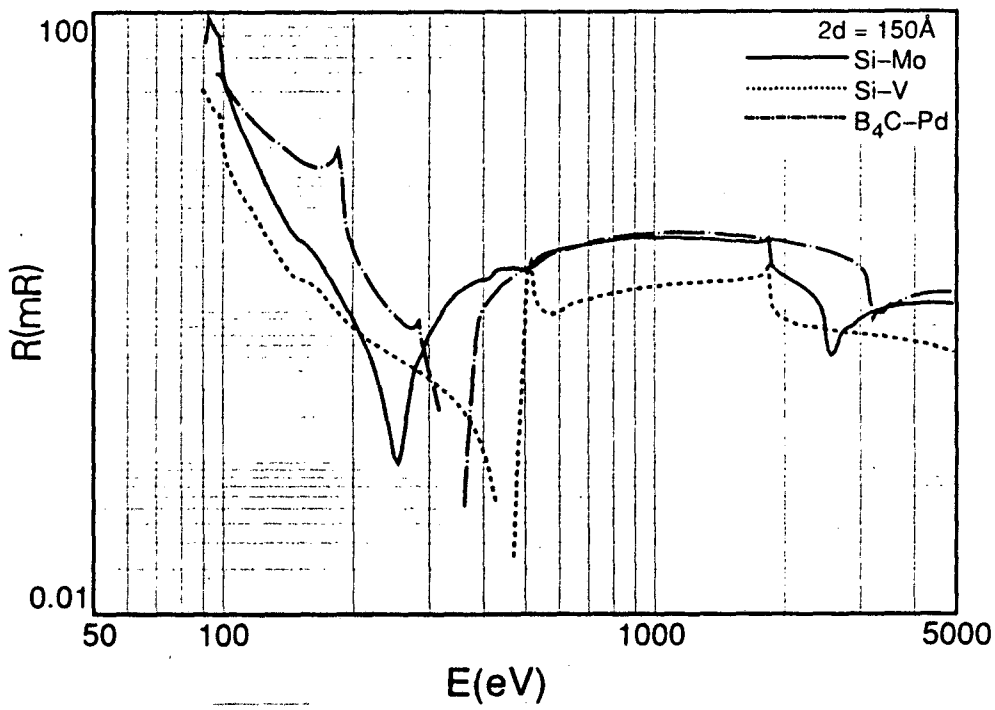

XBL 894-1607

24. Same as for Fig. 23 but with 2d = 150 Å.

To compare directly the integrated reflectivities and optimum energy regions of the selected and optimized multilayers, we present in Fig. 25 R vs E in the 50-2000 eV region embracing the large-angle (10°-80°) first-order diffraction application segments for SiMo150, $B_4CPd100$, PbSt100, CW50, KAP (26.6 Å) and Mica (19.9 Å). For the sputtered multilayers we use the semi-empirically determined interface structure given in Table 3 and a volume fraction of 0.4 for the heavy constituent. The complete reflectivity characterizations R, ω, P and E/ΔE, for these examples of optimized sputtered multilayers are presented in Fig. 26.

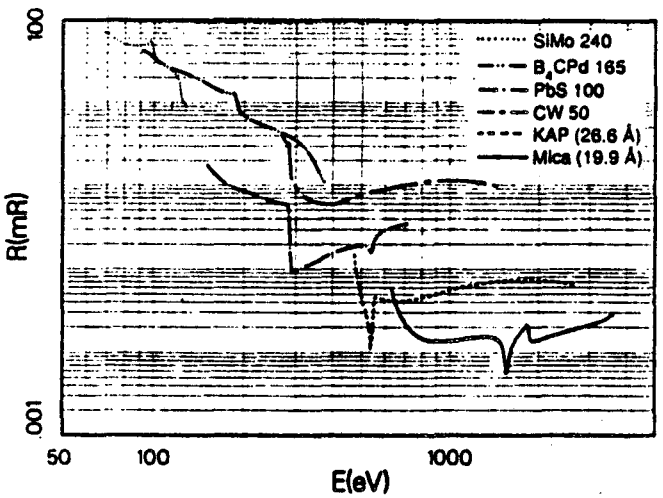

25. Comparing R vs E in the 50-5000 eV region: plots of the large-angle (10-80 deg) diffraction application segments for SiMo240 ...., $B_4CPd165$ -.-.-.-.-, PbSt100 -.-.-.-, CW50 ___-_-___-, KAP(26.6 Å) ---, and Mica(19.9 Å) ___. (Sputtered multilayers with chosen optimal d-spacings and with nominal linear transition interface values of T_1 and T_2 given in Table 3 and with volume fractions of heavy constituent equal to 0.4 and N = 100 layer pairs).

XBL 897-7678

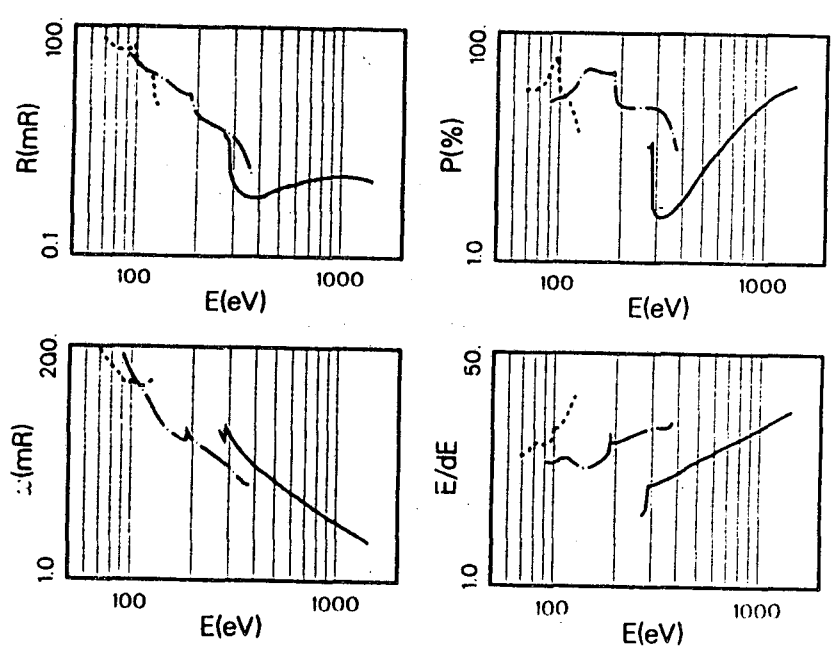

XBL 895-1788

26. Complete semi-empirical reflectivity characterizations of the three selected sputtered multilayers presented in Fig. 25. R, P, ω and E/ΔE, for SiMo240 ---, $B_4CPd165$ -.-.- and CW50 ___.

As an example of an optimized design of a multilayer analyzer for reflection at normal incidence we present in Fig. 27 MDP reflectivity curves around 90° incidence for a Si-Mo multilayer that is "tuned" by varying the d-spacing to yield a peak reflectivity at normal incidence for x radiation of 131 Å (of particular interest in the current x-ray laser development). The parameters for this practical multilayer are: T_1 = 10 Å, T_2 = 20 Å, Y_s/d = 0.4, N = 100 and 2d = 269.5 Å.

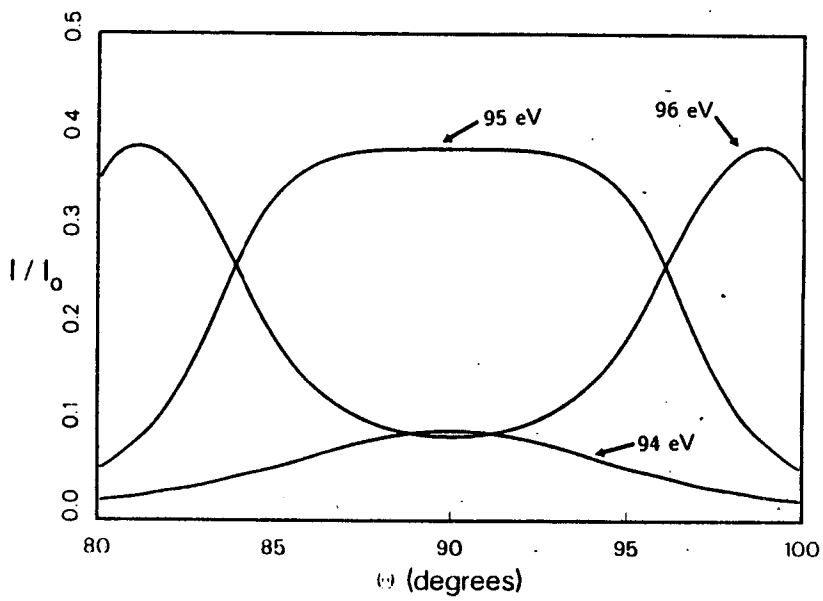

XBL 894-1606

27. Normal-incidence reflectivity for the Si-Mo multilayer, "tuned" in d-spacing for 131 Å radiation. T_1 and T_2 semi-empirically determined to be 10 Å and 20 Å. N = 100.

B. Absolute Spectrometry

In the application of multilayer analyzers to absolute spectrometry one needs to transform a measured x-ray spectrum to an absolute spectrum. Typically, this may be accomplished using a small laboratory computer and relations that follow from those given in (4) and (5). As an example, we consider the transformation of an emission line spectrum that is obtained during a measured time interval, τ, (e.g., per sec, per microsecond burst, etc.) and recorded by a suitable time-integrating detection mechanism, assumed here to be photographic. We will also assume a "point source" geometry (a small physical source or a slit of small dimensions in front of an extended source as required for dispersive spectroscopy). The absolute emission line intensity (at a point source or at a short slit in photons/stearadian) and at photon energy, E, is defined here as $i_o(E)$.

The differential solid angle of the radiation from the source to the multilayer is equal to $\psi\, d\chi$, where ψ is measured in the plane normal to the reflection plane and χ is the emission angle from the source in the plane of reflection as depicted in Fig. 3. The differential angle, $d\chi$, is then related to the corresponding differential range in Bragg angle, $d\theta$, at the multilayer by $d\chi/d\theta$, where $d\chi/d\theta$ is a geometric function derived for a particular cylindrical curvature of the multilayer analyzer (convex, flat or concave). $d\chi/d\theta$ is unity for the flat multilayer illustrated in Fig. 3.

The number of photons, N_x, that is reflected by the multilayer to the detector within a particular diffracted source emission line is given by:

$$N_x = K_1 i_o \psi \int (d\chi/d\theta) I(\theta - \theta_o)\, d\theta = K_1 i_o \psi d\chi/d\theta R \tag{48}$$

where K_1 is the product of the transmission of a filter-window at the source and of that for any primary monochromator (e.g. a mirror). The corresponding photon energy for this emission line is given by the measured diffraction angle using the refraction-corrected Bragg equation.

This reflected number of photons, N_x, may, in this example, be measured by the micro-densitometry of the diffraction line recorded on a suitable photographic film by the relation:

$$N_x = K_2 l \int f(D)\, ds \tag{49}$$

where K_2 is the transmission of a filter-window at the film

cassette and f(D) is the photographic response function relating photons/unit area incident at the film to the photographic density, D, at position s along the spectrographic film. The micro-densitometer's effective slit of length l has a width, Δs, that corresponds to the spectrograph's collimation width which is chosen to be small as compared to the diffraction line width. Finally, by equating (48) and (49) we obtain the absolute emission, $i_o(E)$:

$$i_o(E) = \frac{K_2 l \int f(D)\, ds}{K_1 \psi d\chi/d\theta R} \tag{50}$$

where the integration limits bracket the effective line profiles (usually at $\pm 3\omega$ (FWHM) as discussed earlier).

Using the Lorentzian approximation given in (23) for the MDP diffraction line profile we may write for this discrete emission line source, of $i_o(E)$ total number of photons per stearadian, the distribution, $i(\epsilon)$, for the number of photons reflected by the multilayer per unit reflection angle (measured from the refraction-shifted peak position):

$$i(\epsilon) = \frac{N_x(\omega_x/2\pi)}{\epsilon^2 + (\omega_x/2)^2} \tag{51}$$

where the FWHM, ω_x, may now be considered to be the linear sum of the diffraction width ω and of any additional angular width corresponding to an assumed Lorentzian emission line width in energy, e, and equal to (e/E) tan θ (recalling that a fold of two Lorentzians yields another Lorentzian of width equal to a linear sum of widths). The measured profile may also include additional <u>Gaussian</u> broadening resulting, for example, from an instrumental broadening or plasma temperature broadening which may fold to a Voigt distribution if the Gaussian broadening is significant relative to the Lorentzian broadening. Then, as noted in (43) and discussed in detail in [19], the additional Gaussian width is added non-linearly. This simple but effective description of measured line broadening can often provide a precise diagnostic of, for example, plasma temperature and/or pressure of a high temperature plasma source.

Similarly, we can obtain the absolute intensity $S_o(E)$, (photons/stearadian-eV) for a continuum spectral distribution. See detailed procedures for transforming measured to absolute spectral data (by small computer) which have been presented for various types of multilayer optics in [8] and for several appropriate types of photographic films [26, 27 and 28] and in application to laser-produced fusion diagnostics [6 and 7].

As suggested here and in Eqs. (23)-(26), absolute spectrometry depends principally upon the multilayer analyzer through its parameters, integrated reflectivity, R, and its linear absorption coefficient, μ. These may be determined from our compilations of atomic photoabsorption and scattering factor data presented in [16 and 17]. We present in Tables 4 and 5 detailed R vs E values that may be applied when transforming measured to absolute spectral data for the six selected multilayer analyzers which have been plotted in Fig. 25 for the 50-2000 eV region.

Si-Mo		B_4C – Pd		C-W	
d = 120Å		d = 82.5Å		d = 25Å	
T_1 = 10Å		T_1 = 15Å		T_1 = 8Å	
T_2 = 20Å		T_2 = 15Å		T_2 = 8Å	
E(eV)	R(mr)	E(eV)	R(mr)	E(eV)	R(mr)
69.0	69.8	93.0	42.5	275.0	3.490
70.5	67.3	99.0	35.4	300.0	0.928
72.0	63.5	105.0	29.9	325.0	0.693
73.5	60.5	111.0	27.1	350.0	0.617
75.0	57.8	117.0	25.0	375.0	0.593
76.5	55.7	123.0	23.5	400.0	0.595
78.0	53.7	129.0	22.2	425.0	0.628
79.5	52.1	135.0	20.6	450.0	0.682
81.0	50.8	141.0	18.9	475.0	0.732
82.5	50.0	147.0	17.1	500.0	0.772
84.0	49.5	153.0	15.7	525.0	0.811
85.5	49.1	159.0	14.6	550.0	0.845
87.0	48.9	165.0	13.7	575.0	0.867
88.5	49.1	171.0	13.1	600.0	0.890
90.0	49.5	177.0	12.8	625.0	0.923
91.5	50.1	183.0	12.7	650.0	0.963
93.0	50.8	189.0	9.52	675.0	0.991
94.5	51.8	195.0	7.40	700.0	1.010
96.0	53.5	201.0	6.77	725.0	1.030
97.5	56.6	207.0	6.34	750.0	1.050
99.0	46.5	213.0	6.02	775.0	1.070
100.5	38.3	219.0	5.74	800.0	1.090
102.0	34.5	225.0	5.50	825.0	1.100
103.5	32.5	231.0	5.31	850.0	1.110
105.0	31.0	237.0	5.15	875.0	1.120
106.5	29.6	243.0	4.98	900.0	1.130
108.0	28.3	249.0	4.82	925.0	1.130
109.5	27.2	255.0	4.66	950.0	1.140
111.0	26.2	261.0	4.51	975.0	1.140
112.5	25.2	267.0	4.36	1000.0	1.140
114.0	24.3	273.0	4.22	1025.0	1.140
115.5	23.4	279.0	4.08	1050.0	1.140
117.0	22.5	285.0	3.92	1075.0	1.140
118.5	21.6	291.0	3.76	1100.0	1.140
120.0	20.9	297.0	3.59	1125.0	1.130
121.5	15.1	303.0	3.42	1150.0	1.120
123.0	11.6	309.0	3.24	1175.0	1.120
124.5	10.2	315.0	3.04	1200.0	1.110
126.0	9.5	321.0	2.84	1225.0	1.100
127.5		327.0	2.60	1250.0	1.090
129.0		333.0	2.37	1275.0	1.080
130.5		339.0	2.15	1300.0	1.070
132.0		345.0	1.93	1325.0	1.050
133.5		351.0	1.71	1350.0	1.040
135.0		357.0	1.51	1375.0	1.020
136.5		363.0	1.33	1400.0	1.010
138.0		369.0	1.19	1425.0	1.000
139.5		375.0	1.10	1450.0	

4. R vs E values semi-empirically determined for the selected practical sputtered multilayers , SiMo240, $B_4CPd165$ and CW50 for photon energies corresponding to large-angle first-order diffractions of 10° to 80°.

Lead Stearate	
d = 50Å	
α = .8	
E(eV)	R(mr)
150.0	1.400
180.0	0.751
210.0	0.580
240.0	0.485
270.0	0.451
300.0	0.083
330.0	0.094
360.0	0.108
390.0	0.124
420.0	0.138
450.0	0.147
480.0	0.155
510.0	0.154
540.0	0.127
570.0	0.219
600.0	0.249
630.0	0.269
660.0	0.284
690.0	0.295
720.0	0.307
750.0	0.319
780.0	0.330
810.0	0.339
840.0	0.347
870.0	0.353
900.0	0.359
930.0	0.367
960.0	0.374
990.0	0.379
1020.0	0.383
1050.0	0.387
1080.0	0.390
1110.0	0.391
1140.0	0.392
1170.0	0.393
1200.0	0.393
1230.0	0.393
1260.0	0.392
1290.0	0.391
1320.0	0.390
1350.0	0.389
1380.0	0.387
1410.0	0.385
1440.0	0.383
1470.0	0.381
1500.0	
1530.0	
1560.0	
1590.0	

KAP (001)	
d = 13.31500Å	
E(eV)	R(mr)
500.0	0.0476
550.0	0.0371
600.0	0.0432
650.0	0.0417
700.0	0.0419
750.0	0.0436
800.0	0.0459
850.0	0.0482
900.0	0.0504
950.0	0.0531
1000.0	0.0561
1050.0	0.0586
1100.0	0.0610
1150.0	0.0630
1200.0	0.0649
1250.0	0.0666
1300.0	0.0681
1350.0	0.0695
1400.0	0.0706
1450.0	0.0715
1500.0	0.0723
1550.0	0.0729
1600.0	0.0734
1650.0	0.0738
1700.0	0.0740
1750.0	0.0741
1800.0	0.0741
1850.0	0.0741
1900.0	0.0740
1950.0	0.0738
2000.0	0.0731
2050.0	0.0725
2100.0	0.0721
2150.0	0.0719
2200.0	0.0713
2250.0	0.0708
2300.0	0.0702
2350.0	0.0695
2400.0	0.0689
2450.0	0.0682
2500.0	0.0674
2550.0	0.0667
2600.0	0.0659
2650.0	0.0652
2700.0	
2750.0	
2800.0	
2850.0	
2900.0	
2950.0	

Mica (002)	
d = 10.0049Å	
E(eV)	R(mr)
660.0	0.0336
720.0	0.0194
780.0	0.0154
840.0	0.0140
900.0	0.0136
960.0	0.0136
1020.0	0.0139
1080.0	0.0143
1140.0	0.0147
1200.0	0.0151
1260.0	0.0154
1320.0	0.0154
1380.0	0.0152
1440.0	0.0142
1500.0	0.0117
1560.0	0.0059
1620.0	0.0116
1680.0	0.0150
1740.0	0.0177
1800.0	0.0207
1860.0	0.0153
1920.0	0.0137
1980.0	0.0140
2040.0	0.0145
2100.0	0.0149
2160.0	0.0154
2220.0	0.0158
2280.0	0.0163
2340.0	0.0167
2400.0	0.0171
2460.0	0.0176
2520.0	0.0180
2580.0	0.0184
2640.0	0.0188
2700.0	0.0192
2760.0	0.0196
2820.0	0.0200
2880.0	0.0204
2940.0	0.0208
3000.0	0.0213
3060.0	0.0217
3120.0	0.0222
3180.0	0.0227
3240.0	0.0232
3300.0	0.0238
3360.0	0.0245
3420.0	0.0254
3480.0	0.0266
3540.0	0.0285
3600.0	0.0276

5. R vs E values for PbSt(100Å), KAP(26.6Å) and Mica(19.9Å) for photon energies corresponding to large-angle first-order diffraction of 10° to 80°.

ACKNOWLEDGEMENTS

We gratefully acknowledge the invaluable assistance of the many students and colleagues who have contributed to this program through the past years. In particular, for their assistance in the specific work reported here, we thank D.T. Attwood, P. Batson, J.C. Davis, J.B. Kortright, R.C.C. Perera, R.E. Tackaberry, J.H. Underwood and H.T. Yamada of the Center for X-Ray Optics- LBL; R.H. Day, M.P. Hockaday and R.G. Hockaday of P-14 - LANL; R. Kaufman, of the Y Division - LLNL; D.K. Bradley, P.A. Jaanimagi, J.P. Knauer and M.C. Richardson of the Laboratory for Laser Energetics, U. of Rochester; J.L. Wood of Ovonic Synthetic Materials - ECD. This program is currently supported by the Department of Energy under contracts, SAN # CID # 9501 Task 1 with LANL and LLNL, and with the Director, Office of Energy Research, Office of Basic Energy Sciences, Materials Sciences Division, under Contract No. DE-AC03-76SF00098.

APPENDICES

APPENDIX A - Form Factor Correction for f_1

For the higher photon energies of interest here, we may no longer consider the atoms within a multilayer as "point" scatterers and often must take into account the angle-dependent diffraction by the charge distribution around the nuclei, i.e. by applying the <u>form factor correction</u> given in (11) which reduces somewhat the f_1 component. We have derived (11) in [16] following a suggestion by James [13].

In order to illustrate the accuracy of this simple form factor correction, we compare in Figs. A1 and A2 our corrected f_1 vs E curves for the carbon and neon atoms (based upon our semi-empirical, Kramers-Kronig calculated f_1 tables [16,17] and the tabulated f_o, form factor values given in [15]) to the theoretical f_1 values presented by Kissel, Pratt and Roy [29] (based upon ab initio calculations using the relativistic, 2nd order S-Matrix model). These plots, presented for a scattering angle (2θ) of 90°, are to be compared with the tabulated f_1 curves which correspond to scattering at zero angle (hence requiring no form factor correction) and illustrate the anglular dependence for large angle scattering and high photon energies.

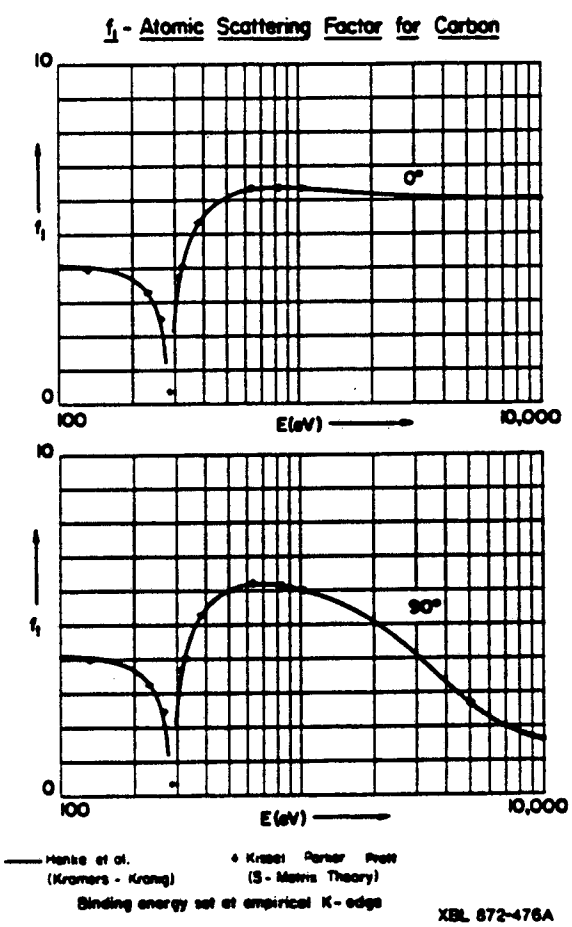

A1. For the larger scattering angles (2θ) and higher photon energies, the real part of the tabulated atomic scattering factors (e.g., in our tables, [16] and [17]) must be reduced to account for an angle-dependent diffraction by the atom's electron "cloud" about its nucleus. Compared here for the <u>Carbon</u> atom are the corrected f_1 curve for 90 deg scattering using the simple form-factor correction presented in (11) and that for 0 deg scattering as we have tabulated in [16] and [17]. Also illustrated here is the excellent agreement with the reduced f_1 values (+) that have been calculated by an accurate, ab initio theoretical model (relativistic, 2nd order S-Matrix theory by Kissel et al. [29]). This form-factor correction is usually significant when $\sin 2\theta/\lambda > 0.1$.

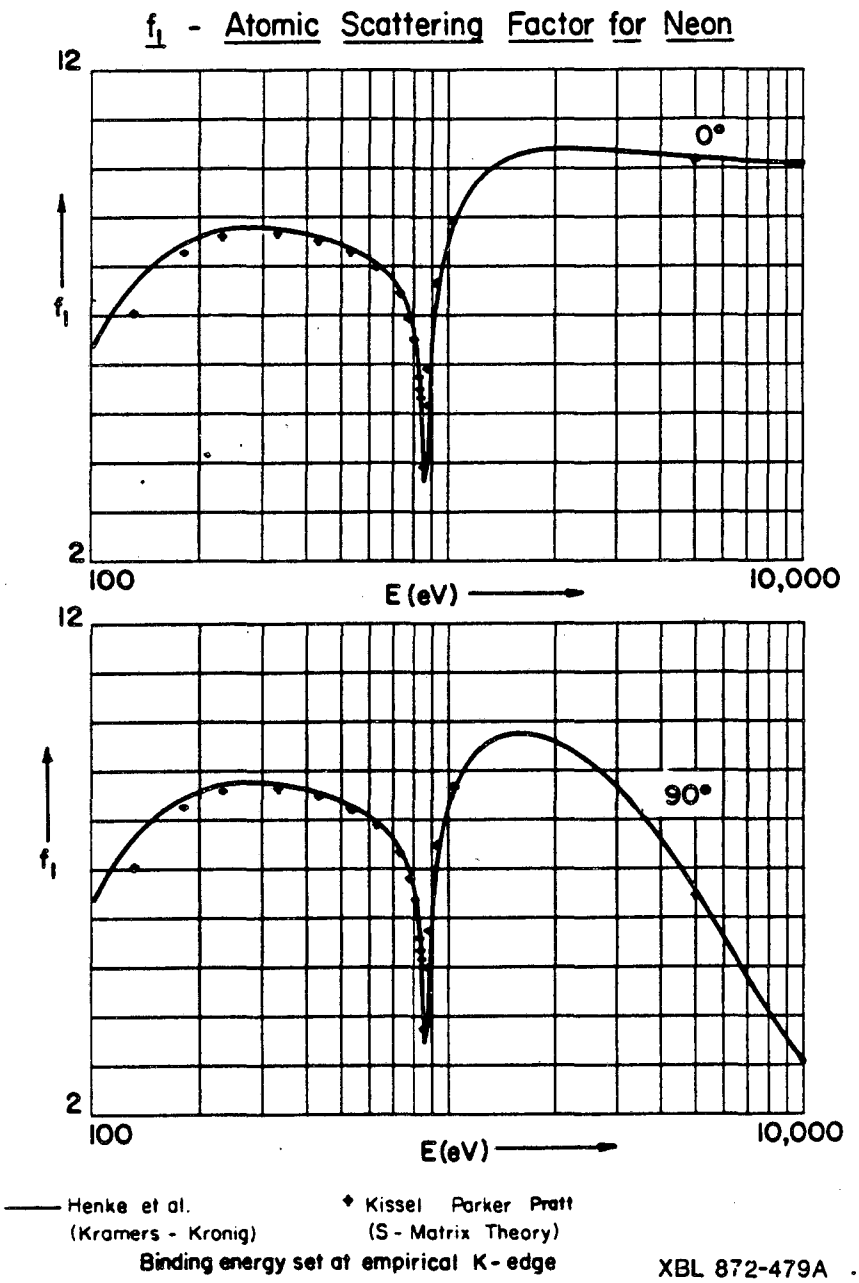

A2. Comparison, for the Neon atom, of the form-factor corrected f_1 values for $2\theta = 90$ deg using (11) and f_1 for $\theta = 0$, as tabulated, with the values calculated by the S-Matrix theory as noted in Fig. A1 for the Carbon atom.

APPENDIX B - Finite Crystal, Modified Darwin-Prins Model

As noted in part B of Sect. III, the Darwin-Prins (DP) solution establishes that the phase and effective reduction of the net amplitude for a wave propagating into the semi-infinite crystal through N layers may simply be expressed as $T_o x^N$, x being given by the relation:

$$x = (-1)^m \exp(-\eta)$$

$$\eta = \mp\sqrt{s^2 - (\sigma + \xi)^2} \qquad (B1)$$

and is the result of the contributions from all possible multiple reflections and transmissions occurring within the semi-infinite multilayer. (The + or - sign for η is chosen by the physical requirement that its real part be positive.)

The amplitude reflection ratio at the Nth layer, corresponding again to a boundary at an infinitely deep crystal, must also be S_o/T_o, and therefore the upward propagating wave amplitude at the Nth layer must be $S_o x^N$ as depicted in Fig. B1 (A). In order to obtain the reflection ratio for a finite multilayer of N layers, we need to eliminate the boundary condition of an effect of the wave interaction of the infinite multilayer below the Nth layer. Let us reverse the roles of downward and upward waves in Fig. B1 (A) by inverting the reflection geometry of (A) as shown in (B). Now by multiplying each boundary wave amplitude indicated in (B) by the same constant factor, $S_o x^N/T_o$, we obtain another consistent set of values for the boundary wave amplitudes, as depicted in (C), with an incident wave from below of amplitude $S_o x^N$ and which is now identical to that in (A).

We next subtract, by a superposition, the two boundary wave solutions depicted in (A) and (C), obtaining the corresponding boundary amplitudes indicated in (D) and with the net upward propagating wave at the lower boundary equal to zero, the required boundary condition for the finite multilayer of N layers.

Finally, by dividing each amplitude in (D) by the incident amplitude, $T_o(1 - (S_o/T_o)^2 x^{2N})$ we obtain the amplitude ratio for finite multilayer reflection and for finite multilayer transmission as was given in (19) and (20), viz.:

$$S_{oN}/T_o = (S_o/T_o)\frac{1 - x^{2N}}{1 - (S_o/T_o)^2 x^{2N}} \qquad (B2)$$

and

$$T_{oN}/T_o = \frac{[1 - (S_o/T_o)^2]x^N}{1 - (S_o/T_o)^2 x^{2N}} \qquad (B3)$$

MODIFIED DARWIN-PRINS (MDP) FOR N LAYERS

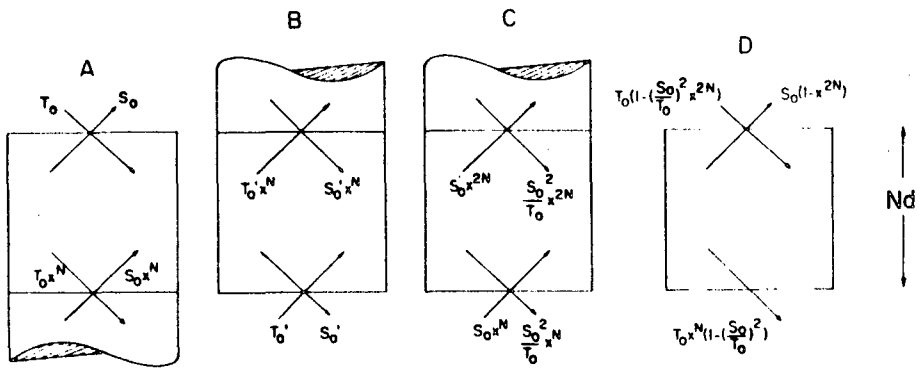

$$x = (-1)^m \exp(-\eta)$$

where $\eta = \mp\sqrt{S^2 - (\sigma + \xi)^2}$

$$S_{ON}/T_0 = (S_0/T_0)(1 - X^{2N})/(1 - (S_0/T_0)^2 X^{2N})$$

$$T_{ON}/T_0 = [1 - (S_0/T_0)^2] X^N/(1 - (S_0/T_0)^2 X^{2N})$$

XBL 858-3318

B1. Illustrating the superposition of particular solutions of the Darwin-Prins model for the semi-infinite crystal in order to obtain the reflected and transmitted amplitudes for a finite crystal of N layers (included in the Modified Darwin-Prins model).

These analytical results combined with (16) above can be easily and rapidly applied for the computation of finite multilayer reflectivity using a small laboratory computer having a complex number arithmetic capability[30]. Generally this analytical MDP model is considerably more adaptable and flexible and requires considerably less computational time than the usual optical E&M (OEM) programs, as has been discussed earlier.

APPENDIX C - Characterizing Multilayer Low-Angle Diffraction and Reflection

A. Low-Angle Diffraction

As discussed in Sec.III, usually the optimum angular range for the application of multilayer analyzers is at the larger angles, typically 10° to 80° Bragg angles. Occasionally, however, it is of interest to utilize a low-angle diffraction from the multilayer, using a sufficiently large d-spacing to place the diffraction line where the total reflection region would normally be. An important example of low-angle diffraction is for synchrotron radiation primary monochromator mirrors, where large d-spacing reflective multilayer coatings can extend the low-angle reflection region and indroduce some band-pass reflectivity enhancement [31].

For the design and characterization of low-angle diffraction mirrors we choose a combination of elements (for sputtering) that will maximize $|A|^2$ in (37) for the wavelength region to be enhanced. We then determine semi-empirically, as described above, the T_1 and T_2 values for this multilayer's transition regions using conventional large-angle diffraction measurements (with sufficiently small d-spacings) for which our MDP semi-empirical modeling is precise. Finally, we choose a large d-spacing that places the diffraction region at the desired low-angles (often set by mechanical constraints of the synchrotron radiation beamlines). Using the optical E&M model with the transition layers expressed by "stepped" profiles as discussed earlier [11], predicted I vs θ reflectivity curves for the required wavelength may be plotted for various values of d-spacing in order to determine a d-spacing that presents a strong first-order diffraction for an allowed reflection angle. Finally, with d and θ so chosen, an energy response curve may be generated which can then establish the mirror's band-pass characteristic.

As an example for the design of a synchrotron radiation monochromator we consider a low-angle diffraction mirror that presents a band-pass at the low-energy side of the oxygen-K absorption edge, around 525 eV (a radiation energy that is strongly absorbed in organic material but not by oxygen-rich materials, e.g. within the "water window"--useful for important applications in x-ray microscopy, microradiography and microlithography.) A typical beam geometry for the new low-energy synchrotron radiation sources (proposed in [32] for the Advanced Light Source (ALS) of the Lawrence Berkeley Laboratory) is about 2.5 mr in $\Delta\theta_s$ and about 5 mr of the "fan" in ψ. (See Fig. 3.) Because 2.5 mr may usually be considered small compared to the FWHM of a first-order diffraction by a sputtered multilayer at 500 eV, we may describe the reflected intensity per

unit energy, dN/dE, of the multilayer by :

$$dN/dE = S_o(E)\ \psi\ \Delta\theta_s\ I(\theta_{bp},\ E)$$

where $S_o(E)$ is the number of photons/sec-eV-steradian in the incident beam at photon energy E from the "white" synchrotron radiation source, and $I(\theta_{bp},E)$ is the reflectivity at the fixed band-pass Bragg angle of the multilayer. In Fig. C1 we have plotted $I(\theta_{bp},E)$ vs E for a C-W multilayer fixed at θ = 10 deg for a first-order 525 eV reflection with a d-spacing of 75 Å. ($T_1 = T_2 = 8$ Å, $Y_s/d = 0.4$ and N = 100.) Usually the effect of $S_o(\theta_{bp},E)$, which includes the transmission of a filter-window of the source, can essentially eliminate the low energy component of this response curve. The beam cross section will be $\ell\psi \times \ell\Delta\theta_s$, where ℓ is the total source-to-multilayer-to-work chamber distance.

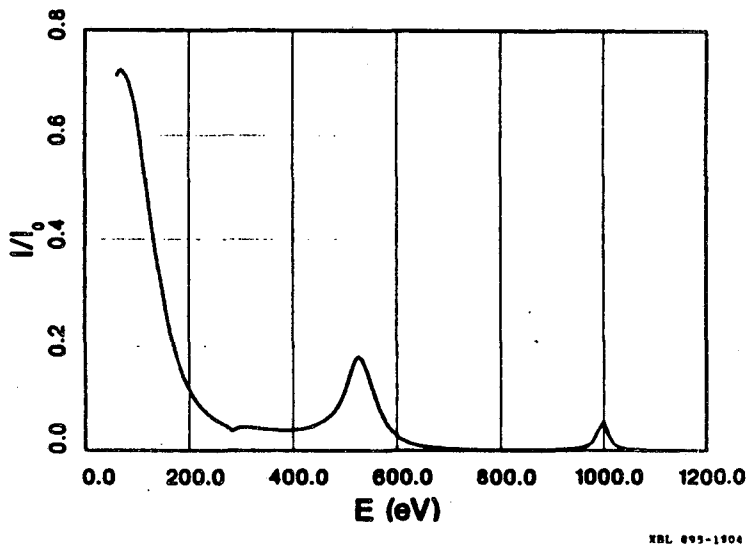

C1. The photon energy response, I/I_o vs E, of a C-W multilayer designed to provide a band-pass at 525 eV as a primary monochromator for a synchrotron radiation source having a divergence in the reflection plane that is small compared to its diffraction line width (providing an effective radiation for quantitative x-ray microscopy and microradiography of organic materials). Because it requires a calculation through the total reflection region to evaluate its low-energy transmission background, the optical E&M model must be applied here. A d-spacing of 75 Å was chosen, placing the 525 eV band-pass at 10 deg. The calculation uses the nominal interface transition layer thicknesses given in Table 3, T_1=T_2=8 Å, and a heavy element volume fraction Y_s/d = 0.4 and N = 100.

An OEM model calculation for $I(\theta_{bp},E)$) was required for the low-angle diffraction involved in Fig. C1 (using a small computer program described in [11]). Our more convenient analytical MDP model program [30] <u>cannot</u> be applied to calculate low-angle reflectivity characteristics because, as noted earlier, its parameters, σ and s, must have magnitudes that are small as compared to unity in order to yield a solution of the difference equations that leads to the analytical result (16). It may readily be shown as follows that this limit on σ and s corresponds to having the first-order diffraction line at angles greater than about $3\theta_c$.

The critical angle for the "total reflection" cut-off is defined as that angle at which the intensity drops to half of its low angle limit, I_o. This critical angle, θ_c, is given, within a good approximation [31] by:

$$\sin\theta_c = \sqrt{2\delta} \tag{C1}$$

The analytical Darwin-Prins solution for reflected amplitude (16) was obtained by letting σ and s be small as compared to unity [given in (12) and (13)]. Since s is always smaller than σ, we need only require that σ be small. From (12), we may write for the approximate magnitude of σ:

$$|\sigma| \approx r_o\lambda\frac{MF_1(0)}{\sin\theta} \tag{C2}$$

where we have neglected $F_2(\theta)$, which is relatively small except at certain threshold energies. (Modeling cannot be applied at these energies in any event.) We may write for δ, using (22):

$$\delta = \frac{r_o\lambda^2}{2\pi}\frac{MF_1(0)}{d} \tag{C3}$$

Combining these relations with the Bragg relation for first-order diffraction ($\sin\theta_1 = \lambda/2d$), we obtain the approximate result:

$$\frac{\theta_c}{\theta_1} = \sqrt{\frac{2\sigma}{\pi}} \tag{C4}$$

Letting $\sigma = 0.2$, we obtain a convenient "rule of thumb" for the smallest angle allowed for a first-order diffraction profile that may be accurately described by the MDP model:

$$\theta_1 > 3\theta_c \tag{C5}$$

The accuracy of the MDP solution for diffraction at angles greater than $3\theta_c$ has been illustrated in Figs. 2, 8 and 9.

B. Low-Angle Fresnel Reflection

For θ_1 larger than $3\theta_c$ and correspondingly for σ and s small compared to unity, the MDP model accurately describes the multilayer reflectivity in the low-angle "total reflection" region. We show as follows that the MDP description reduces identically to the Fresnel specular reflection equations at the

small angles:

In the small angle region, we note from (12) and (13) that the parameters σ and s become equal and the expression for the reflected amplitudes, So/To, given in (16) reduces to:

$$S_o/T_o = \frac{-\sigma}{(\xi+\sigma)+\sqrt{\xi^2+2\xi\sigma}} \qquad (C6)$$

where now $\xi = 2\pi d \sin\theta/\lambda$, since this small angle "region of interest" is defined by letting $\sin\theta_o$ (equivalently, the diffraction order, m) be equal to zero in (17).

The Fresnel equation or the amplitude ratio reflected at the small angles may be given by (see, for example Eq. 4.84 of James [13]):

$$S_o/T_o = \frac{\sin\theta - \sqrt{\sin^2\theta - 2\alpha}}{\sin\theta + \sqrt{\sin^2\theta - 2\alpha}} \qquad (C7)$$

where $\alpha = \delta + i\beta$.

Multiplying the numerator and denominator of (C7) by the denominator gives the result:

$$S_o/T_o = \frac{\alpha}{\sin^2\theta - \alpha + \sin\theta\sqrt{\sin^2\theta - 2\alpha}} \qquad (C8)$$

Now by multiplying (C8) through its numerator and denominator by the factor $2\pi d/(\lambda\sin\theta)$, and using the relations (35) and (13) we obtain a relation which is identical to the MDP result (C6). This was obtained with the assumption that the optical constants (δ and β) are the average values for the multilayer system. Generally the penetration depth at "total reflection" [33] will include a sufficient number of layer-pairs (necessarily "thin" for multilayer analyzers) to allow the "bulk" values for δ and β to be applicable. This is demonstrated by the generally close agreement between the low-angle reflectivity curves that are calculated by the zero-order MDP model and by the OEM model, where the latter is calculated for the two possible systems, with the heavy layer <u>and</u> the light layer at the surface. The curves differ significantly only for the larger d-spacing multilayers applied at x-ray wavelengths which place the first-order diffraction line near the reflection cut-off region (i.e. when θ_1 is less than $3\theta_c$).

Comparing the MDP low-angle reflection characteristic (with θ_1 greater than $3\theta_c$) to that measured can be a useful check on

surface structure and the multilayer's optical constants.

APPENDIX D - The Kinematical (with Absorption) Multilayer Model

In this appendix we present a derivation of a kinematical model using the difference equations defined in Fig. 7. It is shown that the relative reflected intensity has a Lorentzian line profile. The integrated reflectivity is shown to be equal to the integrated reflectivity of the Mosaic crystal model. Expressions are derived for the peak reflectivity and diffraction line width.

Following Darwins approach[13] we write a set of difference equations for the upward, S_r, and downward, T_r, propogating waves above the rth layer in a semi-infinite multilayer as shown in Fig. 7. The second term in the equation for T_{r+1} results from the downward reflection of the upward propagating (i.e. previously reflected) wave, S_{r+1}. By neglecting this term we effectively ignore multiple reflections and arrive at a kinematical model. The difference equations then become,

$$S_r = -isT_r + (1 - i\sigma)e^{-i\delta}S_{r+1} \qquad (D1.a)$$

$$T_{r+1} = (1 - i\sigma)e^{-i\delta}T_r \qquad (D1.b)$$

where $\delta = 2\pi d \sin(\theta)/\lambda$. Assuming that $\sigma << 1$ implies that $(1-i\sigma) \approx e^{-i\sigma}$ and Eq. (D1.b) becomes

$$T_r = e^{-ir(\delta+\sigma)}T_o \qquad (D2)$$

If we consider a multilayer with N layers then $S_N = 0$, and using Eqs. (D1.a) and (D2) we may solve for S_{N-1} and S_{N-2},... until finally one obtains for S_o,

$$S_o = -is[1 + e^{-i2(\delta+\sigma)} + e^{-i4(\delta+\sigma)} + \cdots + e^{-i2(N-1)(\delta+\sigma)}]T_o \ . \qquad (D3)$$

which can be expressed as

$$S_o = -isT_o[1 - e^{-i2N(\delta+\sigma)}]/[1 - e^{-i2(\delta+\sigma)}]. \qquad (D4)$$

If we take the limit as N becomes large then, since σ has a negative imaginary part, the expression in the numerator goes to

one. Letting $\delta = m\pi+\xi$ where,

$$\xi = \delta - m\pi = 2\pi d(\sin\theta - \sin\theta_o)/\lambda \qquad (D5)$$

and θ_o is the Bragg angle defined by $m\lambda = 2d\sin\theta_o$, Eq. (D4) becomes,

$$S_o = -isT_o/[1 - e^{-i2(\xi+\sigma)}] \qquad (D6)$$

Now again making the assumptions that both ξ and σ are small compared to unity we obtain the following expression for the ratio of the reflected to the incident amplitudes at the multilayer surface,

$$S_o/T_o = -s/[2(\sigma + \xi)] \qquad (D.7)$$

The reflected intensity is obtained by taking the magnitude of Eq. (D2) squared. For unpolarized radiation we take the average of the intensities for each polarization. This yields a reflectivity which is a Lorentzian as a function of angle and is given in the text equations (23) through (27).

At sufficiently high energies the absorption coefficient becomes small and the peak relectivity given by this model will exceed unity, which, of course, is unphysical. The requirement that the peak reflectivity be less than one provides a limit on the applicability of this kinematical model. This condition is violated when multiple reflections become important, in which case the Modified Darwin-Prins model for the line profile must be used.

APPENDIX E -Determination of the One-Dimensional Crystal Structure

A conventional way to present the three-dimensional unit cell is to use a set of three vectors normally denoted a, b, and c with magnitudes a, b, and c, and with the included angles α, β, and γ. The coordinates relative to this basis set of individual atoms are usually designated x', y' and z' (z' is usually different from z as used here). Formulae for the determination of the z-coordinates of the atoms (hence the one-dimensional distribution) from the general coordinate values are presented below.

Generally it is necessary to search the crystallographic literature to find these coordinate values. A good source of such data is Crystal Structures by Wyckoff [34]. However, its notation is very compact, and the reader is encouraged to read its Introduction carefully. For further help in understanding the notation used, and for a good general reference, see the International Tables for X-Ray Crystallography [35]. Finally, for a very helpful "consistency" check, the mass density of an assumed unit cell should be calculated and compared to the bulk density of the crystal.

The specific crystal planes being used are normally specified by their Miller indices (h,k,l). When these indices and the unit cell's dimensions a, b and c, are known along with the atomic coordinates, x', y' and z', the following relations, involving the unit cell volume V, may be applied to define the needed multilayer structural parameters:

$$V = abc\sqrt{1 + 2\cos\alpha\cos\beta\cos\gamma - \cos^2\alpha - \cos^2\beta - \cos^2\gamma} \qquad (E1)$$

$$\begin{aligned}(V/d)^2 = {} & h^2b^2c^2\sin^2\alpha + k^2a^2c^2\sin^2\beta + l^2a^2b^2\sin^2\gamma \\ & +2hk(abc^2)(\cos\alpha\cos\beta - \cos\gamma) \\ & +2kl(a^2bc)(\cos\beta\cos\gamma - \cos\alpha) \\ & +2lh(ab^2c)(\cos\gamma\cos\alpha - \cos\beta)\end{aligned} \qquad (E2)$$

from which we may determine the cross-sectional area, α, and the d-spacing.

The one-dimensional z/d coordinates are given by:

$$z/d = hx' + ky' + lz' \qquad (E3)$$

A constant may be added to these coordinates to have z = 0 correspond to a symmetry plane. Note: For crystals having a hexagonal unit cell, often four-component Miller indices are given; this notation may be converted to normal Miller indices by neglecting the third component.

In Tables E1 and E2 are presented our calculations [36] for the one-dimensional structural parameters for the cleavage planes of the multilayers, mica and KAP, along with those for other analyzers generally used for x-ray spectroscopy.

Mica (002)	
d = 10.0049Å	A = 93.3735Å^2
Z/d	no.
K^+	
±.5000	2
$Al^{+1.5}$	
±.0032	2
±.2744	1
±.7256	1
±.9968	2
H	
±.1040	2
±.8960	2
Si^{+2}	
±.2730	2
±.2744	1
±.7256	1
±.7270	2
O^-	
±.1040	2
±.1054	2
±.1084	2
±.3240	2
±.3348	2
±.3360	2
±.6640	2
±.6652	2
±.6760	2
±.8916	2
±.8946	2
±.8960	2

Table E1

E1. Unit cell one-dimensional structure (atomic z/d position), d and cross-section for the (002) cleavage plane reflection of Muscovite Mica, needed for the calculation of MF using (14).

KAP (001)	
d = 13.3150Å	A = 62.013Å^2
Z/d	no.
K^+	
±.0388	2
O	
±.1440	2
±.0931	2
±.1273	2
±.2626	2
C	
±.2584	2
±.3251	2
±.4205	2
±.4505	2
±.3847	2
±.2894	2
±.1569	2
±.2176	2
H	
±.3030	2
±.4640	2
±.5210	2
±.4000	2
±.2350	2

Table E2

E2. Unit cell one-dimensional structure (atomic z/d position), d and cross-section for the (001) cleavage plane reflection of KAP, needed for the calculation of MF using (14).

APPENDIX F - The Langmuir-Blodgett Multilayer: Construction and Structure Determination

The Langmuir-Blodgett (LB) multilayers are constructed by successively depositing N mono-molecular layers of typically a lead or barium salt of a straight-chain fatty acid upon a smooth substrate (e.g. a highly polished glass or a silicon wafer). The resulting multilayer has a periodic structure comprised of thin double atomic layers of the heavy cation (e.g. Pb or Ba) separated by the low density, long carbon-chain matrix providing the desired high x-ray scattering "contrast". The d-spacings are set simply by the choice of the straight-chain fatty acids that can be successfully applied for constructing high quality multilayer analyzers which, from our experiments, are in the 35 to 80 Å range.

In comparison to the atomically densely-packed sputtered-or-evaporated multilayers, the LB multilayers are low-density, low absorbing systems for which the effective number of reflecting layers is appreciably higher. Typically optimized LB multilayer analyzers will have similar peak reflectivities, lower integrated reflectivities and higher resolution than the optimized sputtered-or-evaporated multilayers, thereby complementing well these multilayer analyzers. (The more rugged sputtered multilayers can provide wider band-pass characteristics and can be used at higher radiation loading. For example, these may be the primary monochromators for modern synchrotron radiation sources and may be followed by low energy spectrographs utilizing the higher resolution LB analyzers.)

Our methods of constructing LB multilayer analyzers (which have been developed in this program through two decades) are illustrated in Fig. F1. A monomolecular fatty acid layer is deposited upon an ultra-clean water surface which contains a small concentration of Pb^{++} ions, for example, thereby establishing a monomolecular layer of the lead salt ions of the straight-chain fatty acid. This monomolecular layer is compressed by a floating (Teflon sheet) "piston" as shown. The multilayer substrate is mounted on a high-inertia, balanced rocking arm (mounted from a heavy table supporting the tank) and is driven in and out of the water surface by a constant-speed, reversing motor (micro-switched at dipping limits). The shallow tank is machined from a solid Teflon block about 120 cm long. (An extra block of Teflon is cemented below one end of the tank to allow the machining of a well into which the substrate is dipped.)

Initially, monomolecular layers are deposited upon the substrate on the downstroke <u>and</u> on the upstroke, generating a multilayer defined by Langmuir as the Y-type film. This process is depicted schematically in Fig. F2 which includes a diagram of

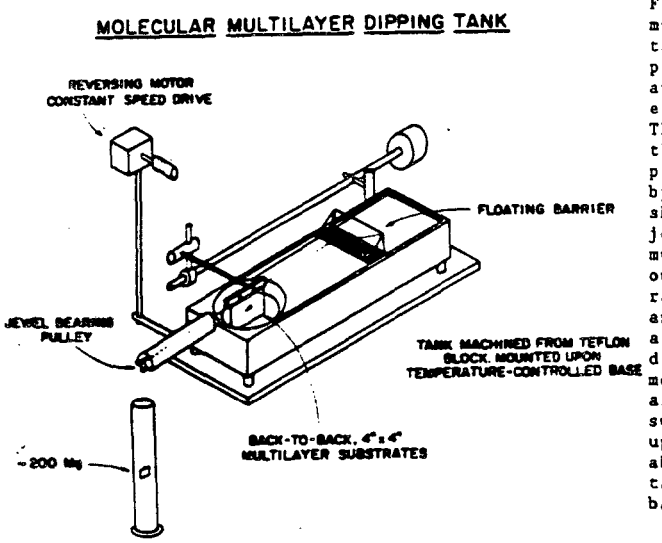

XBL 894-1656

F1. Dipping tank for constructing Langmuir-Blodgett multilayer analyzers for the 100-1000 eV region. A shallow tank and well is machined in Teflon which is non-wetting and permits using concentrated H_2SO_4-chromate cleaning solution and provides the required positive meniscus that allows efficient sweeping of the water surface with a Teflon bar. The Teflon block is bolted to a massive aluminum base through which chilled or heated water may be circulated to provide temperature control. Surface pressure is maintained by pulling against the deposited monomolecular film a Teflon sheet "piston" with a Nylon thread that passes over a jeweled-bearing pulley to a counter-weight. Back-to-back multilayer substrates are dipped at constant speed in and out of the film surface, driven by a reversing motor that raises and lowers a high inertia rocking arm that is pivoted and balanced by counter weight on a structure which is also attached to the base of the tank. A de-ionized doubly distilled water supply is provided to maintain the positive meniscus by replacing any loss following surface sweeping after each monolayer film has been used up through successive dips. The tank is about 25 by 120 cm and sits upon a slow laminar-flow clean bench. (We have also been able to construct very successful and efficient dipping tanks by machining these directly into an aluminum block base which was then Teflonated.)

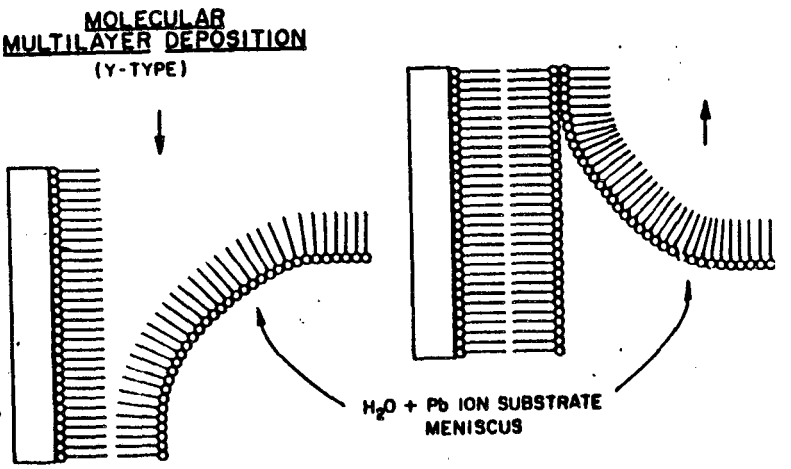

XBL 868-2433

F2. Illustrating the process by which the monolayer is deposited on both the down and up strokes--defining the Y-type film. (When deposition occurs only on the down stroke, it is defined as an X-type film.) Schematically, double stearic chains are shown here as "sticks" oriented nearly normal to the water surface with their hydrophobic CH_3 ends outermost and their hydrophilic carboxyl ends terminating at the surface attaching to a bivalent cation (circles), e.g., the Pb cation. Molecular forces dictate that on the down stroke, the CH_3 ends come together, and on the up stroke a double layer of the cations is formed. In this way a dense layer of the heavy cations (as Pb or Ba) is separated by a light carbon matrix with a d-spacing equal to two stearic molecular chain lengths as shown here.

Table F1

MULTILAYER DEPOSITION CONDITIONS FOR LEAD SALTS OF FATTY ACIDS

COMPOUND	CHEMICAL FORMULA	SOLVENT	SOLUTE CONCENTRATION (mg/ml)	METAL ION CONCENTRATION (M)	SUBPHASE pH	TEMP (°C)	SURFACE PRESSURE (dynes/cm)	DEPOSITION TYPE	RATE OF DEPOSITION (cm/sec) Initial	Subse
Lauric acid	$CH_3(CH_2)_{10}COOH$	hexane (80 v%) +toluene (20 v%)	0.75	Pb^{2+} = 1.7 x 10^{-4} Al^{3+} = 4.4 x 10^{-6}	5.7	20-22	11	Y-film	0.02	0.08
Myristic acid	$CH_3(CH_2)_{12}COOH$	hexane	0.8	Pb^{2+} = 8.5 x 10^{-5} Al^{3+} = 2.2 x 10^{-6}	5.4	21-23	14	X-film	"	0.2
Stearic acid	$CH_3(CH_2)_{16}COOH$	hexane	1.0	"	5.9	23-25	28	"	"	0.2
Behenic acid	$CH_3(CH_2)_{20}COOH$	hexane	0.8	"	5.3	34-36	28	"	"	0.13
Lignoceric acid	$CH_3(CH_2)_{22}COOH$	hexane	0.8	"	5.4	45-47	28	"	"	0.18
Melissic acid	$CH_3(CH_2)_{28}COOH$	Xylenes	0.8	"	5.4	56-60	32	"	"	0.04

Type of Substrate: Float glass, ultrasonically cleaned in "Micro" soap solution and throughly rinsed with hot double distilled water four time

*Rate of deposition: All crystals were initially deposited at a speed of 0.02 cm/sec and the rate of deposition was gradually increased to a value shown under the "subsequent" rate of deposition column.

F1. Typical, optimizing conditions for the construction of molecular multilayer analyzers of lead salts of straight-chain fatty acids, $[CH_3(CH_2)_n(COO)]_2$ Pb for 2d values in the 70 - 160 Å range. (2d = 5.0(n + 4).)

the stearic acid molecule. In our depiction of the formation of the Y-type film, the carbon chains with their hydrophobic carbon tails are shown as line segments and the lead carboxylate, hydrophilic ends of the lead stearate molecule are shown as circles. During a downward stroke, the hydrophobic ends (carbon tails) attach themselves to the carbon tails of the last fatty-acid-salt soap molecules that were previously deposited upon the solid multilayer. During the following upward stroke of the substrate-multilayer, the hydrophilic (lead carboxylate group) ends of the monolayer molecules adhere to the similar polar groups on the outer surface (under water) of the previously deposited layer as depicted here in Fig. F2. In this way, with each up and down cycle, a "heavy" double-lead carboxylate sublayer is generated, separated by a d-spacing equal to <u>two</u> "light" straight-chain molecule lengths.

Invariably, when constructing multilayers with the lead cation (appropriate for constructing our most efficient analyzers) the deposition mode reverts, after a few cycles, to an X-type for which deposition only occurs on the downstroke. Remarkably, the resulting periodic structure of the multilayer is identical to that for the Y-type film deposition described in Fig. F2. Now, however, two in-and-out cycles are required to generate a d-spacing of the structure. In contract to the formation description presented above for the Y-film, that required for the X-film is more complex. For example, see Langmuir [37] and Honig [38] for proposed X-formation models.

The "art" of constructing molecular multilayer analyzers (usually of sub-micron thicknesses on a substrate) involves careful, systematic, ultra-clean laboratory practice. The most easily constructed multilayer analyzers are those that deposit well at room tempratures, viz. the lead salts of myristic, stearic and behenic acids (yielding d-spacings of 40, 50 and 60 Å respectively). Along with tank temperature, the other variables that need to be adjusted are its cation concentration and pH, and the surface (piston) pressure and dipping rate. In Table F1 we present typical construction conditions which we have found suitable for constructing LB multilayers in the 35-80 Å d-spacing range.[39]

The general chemical formula for a salt of a straight-chain fatty acid with the required bi-valent cation (as Pb) may be written:

$$[CH_3(CH_2)_nCOO]_2Pb$$

where n is the number of CH_2 groups between an end CH_3 group and the carboxylate. We have measured the absolute spacing of multilayers generated from a series of fatty acids and have found that the d-spacing may be closely predicted for a given value of

n by:

$$d = 2.5(n+4)\text{Å} \tag{F1}$$

which establishes the projected spacing between the CH_2 groups along the molecule z-axis to be 1.25 Å. We have used available crystalographic data on fatty acids and on the carboxyl groups to assign positions for the other atoms in the fatty acid molecule. These are indicated in Fig. F3.

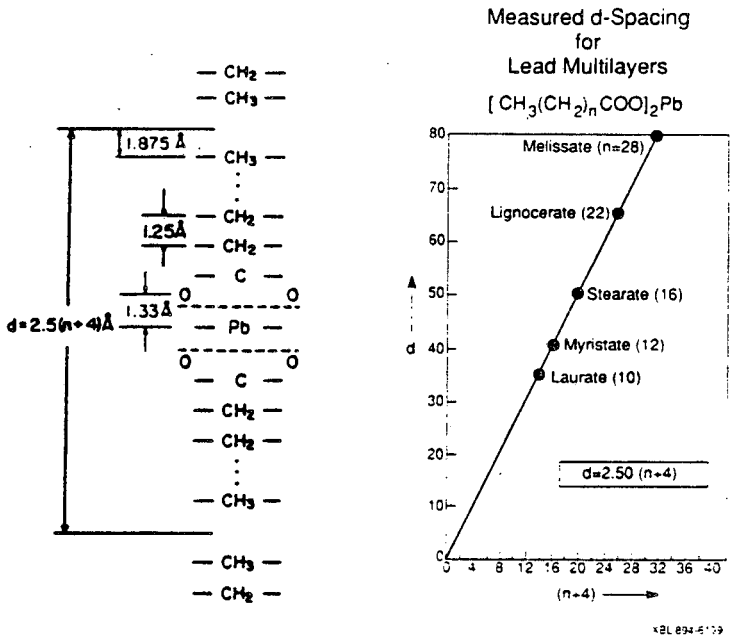

F3. Unit cell for a lead salt of a straight-chain fatty acid -- $[CH_3(CH_2)_n(COO)]_2Pb$, n = 16 for lead stearate (PbSt). The one-dimensional distribution of atoms within the unit cell that is assumed in our modeling is presented here. We have measured the d-spacing for the multilayers generated as salts of the fatty acids to be equal to approximately 2.5(n+4) and the cross-sectional area occupied by a typical film's unit cell to be about 20.5 $Å^2$.

By calculating the z/d positions from the symmetry Pb-layer position, we may drop the second summation (with odd sine terms) in (14) and calculate MF using:

$$MF_1 = \frac{1}{\alpha}\sum_1 x_q f_{1q} \cos\left[\frac{4\pi z_q}{\lambda}\sin\theta\right]$$

$$MF_2 = \frac{1}{\alpha}\sum_1 x_q f_{2q} \cos\left[\frac{4\pi z_q}{\lambda}\sin\theta\right] \tag{F2}$$

where x_q is the number of atoms of species-q at position z_q from the symmetry plane and having atomic scattering factor, f_{1q} + f_{2q}, and the cross sectional area occupied per molecule is α.

We have applied this relation for MF with the measured d-spacings and have varied the area density, M, of the molecules [$=(\alpha)^{-1}$] to semi-empirically fit the measured integrated reflectivity data for a series of molecular multilayers in the 35-80 Å d-spacing range using the modeling procedures presented in Sect. V. Generally, the precision of the fitting through several diffraction orders was found to be well within experimental errors. The unit cell area (molecular cross section) was determined by this fitting procedure to be about 20.5 $Å^2$. An example of these semi-empirical model fits has been presented in Fig. 21 for the lead stearate analyzer.

APPENDIX G - Construction of Sputtered or Evaporated Multilayers

The fabrication of these multilayers has been accomplished with a variety of techniques, such as for example, evaporation[40], magnetron sputtering[41], ion beam sputtering[42], and laser plasma source deposition[43]. A brief description of the most commonly applied methods, magnetron sputtering and evaporation, is given below.

The construction of evaporated multilayers has been developed by Spiller and co-workers at IBM and is reviewed in ref. 40. The substrate is located in front of two evaporation sources which are controlled by means of mechanical shutters. A major problem is with the stabilization of the evaporation rate which is difficult due to the strong dependence of vapor pressure on temperature. This problem was overcome by the use of *in situ* monitoring of the x-ray reflectivity during the multilayer growth.

The most commonly applied technique for multilayer construction, magnetron sputtering, was developed by Barbee and co-workers and is reviewed in ref. 41. The substrate is typically moved on a table between two sputter sources, often rotated at constant velocity. Through the use of stable power supplies, either dc or rf depending on the material being deposited, and control of the sputtering gas pressure, remarkably stable deposition rates are achievable. The thicknesses of the layers are then determined simply by the deposition rates and the time spent over each source.

REFERENCES

1a. M.C. Richardson, G.G. Gregory, R.L. Keck, S.A. Letzring, R.S. Marjoribanks, F.J. Marshall, G. Pien, J.S. Wark, B. Yaakobi, P.D. Goldstone, A. Hauer, G.S. Stradling, Y. Ameduri, B.L. Henke and P.A. Jaanimagi, "Time Resolved X-Ray Diagnostics for High Density Plasma Physics" Laser Interaction and Related Phenomena, Vol. 7, p. 179 (Plenum Publishing 1986).

1b. P.A. Jaanimagi, L. Deletrez, B.L. Henke and M.C. Richardson, "Temporal Dependence of the Mass-Ablation Rate in UV Laser-Irradiated Spherical Targets" *Phys. Rev. A* 34, 1322 (1986).

1c. P.A. Jaanimagi, H. Chen, R.S. Marjoribanks, D.K. Bradley, J.F. Seely, U. Feldman, C. Brown, J.H. Underwood, and B.L. Henke "Space and Time Resolved Diagnostics of Soft X-Ray Emission from Laser Plasmas" *SPIE* 913 (1988).

1d. C.M. Brown, U. Feldman, J.F. Seely, M.C. Richardson, H. Chen, J.H. Underwood, and A. Zigler, "Imaging of Laser Produced Plasmas at 44 Å using a Multilayer Mirror" *Optics Communications* 68, 190 (1988).

2. N.M. Ceglio, D.G. Stearns, D.P. Gaines, A.M. Hawryluk, and J.E.Trebes, "Multipass Amplification of Soft X Rays in a Laser Cavity" *Optics Letters* 13, 108 (1988).

3. G.S. Stradling, D.T. Attwood, R.L. Kauffman, "A Soft X-Ray Streak Camera" *IEEE Journal of Quantum Electronics* QE-19, 604 (1983).

4. R.L. Blake, R.G. Hockaday, J.S. Grosso, G.C. Idzorek, B.L. Henke and J.L. Wood, "Calibrations of a Multichannel Soft X-Ray Spectrometer" SPIE, Vol. 688 (1986).

5a. B.L. Henke, R.C.C. Perera, and D.S. Urch, "Cl-$L_{II,III}$ Fluorescent X-Ray Spectra Measurement and Analysis for the Molecular Orbital Structure of ClO_4^-, ClO_3^- and ClO_2^-," *J. Chem. Phys.* 68, 3692 (1978).

5b. R.C.C. Perera and B.L. Henke, "Multilayer X-Ray Spectrometry in the 20-80 Å Region: A Molecular Orbital Ananlysis of CO and CO_2 in the Gas and Solid States," *X-Ray Spectrometry* 9, 81 (1980).

5c. R.C.C. Perera, C.H. Zhang, T.A. Callcott, and D.L. Ederer, "Electronic Bonding of Buried Interfaces Determined by Soft X-Ray Emission Spectroscopy" *J. Appl. Phys. to be published.*

6. B.L. Henke and P.A. Jaanimagi, "A Two-Channel,

Elliptical Analyzer Spectrograph for Absolute Time-Resolving Time-Integrating Spectrometry of Pulsed X-Ray Sources in the 100-10,000 eV Region," *Rev. Sci. Instrum.* 56, 1537 (1985).

7. P.A. Jaanimagi, B.L. Henke and M.C. Richardson, "An Absolutely Calibrated Time-Resolving X-Ray Spectrometer," *Proc. of the SPIE* 569, 159 (1985).

8. B.L. Henke, H.T. Yamada and T.J. Tanaka, "Pulsed Plasma Source Spectrometry in the 80-8000 eV X-Ray Region," *Rev. Sci. Instrum.* 54, 1311-1330 (1983).

9. J.H. Underwood and T.W. Barbee, Jr., "Layered Synthetic Microstructures as Bragg Diffractors for X-rays and Extreme Ultraviolet: Theory and Predicted Performance," *Appl. Opt.* 20, 3027 (1981).

10. E. Spiller and A.E. Rosenbluth, "Determination of Thickness Errors and Boundary Roughness from the Performance of a Multilayer Coating," Proceedings of SPIE - The International Society for Optical Engineering, Vol. 563, 221 (1985).

11. H.T. Yamada, J.C. Davis, E.M. Gullikson and B.L. Henke, "A Program for the Optical E&M Modelling of Multilayer X-ray Analyzers"- *In Preparation.*

12. B.L. Henke, J.Y. Uejio, H.T. Yamada, and R.E. Tackaberry, "The Characterization of Multilayer X-Ray Analyzers: Models and Measurements," *Opt. Engin.* 25, 937 (1986).

13. R.W. James, The Optical Principles of Diffraction of X-Rays (Cornell University Press, Ithaca, New York, 1965).

14. A.H. Compton and S.K. Allison, X-Rays in Theory and Experiment, 2nd ed. (Van Norstrand, New York, 1935).

15. J. H. Hubbell and I. Overbo, *J. Phys. Chem. Ref. Data* 8, 69 (1979).

16. B.L. Henke, P. Lee, T.J. Tanaka, R.L. Shimabukuro, and B.K. Fujikawa, "Low-Energy X-Ray Interaction Coefficients: Photoabsorption, Scattering and Reflection," *Atomic Data and Nuclear Data Tables* 27, No. 1 (1982).

17. B.L. Henke, E.M. Gullikson, J.C. Davis and R.C.C. Perera, "Low Energy X-Ray interaction Coefficients: Photoionization, Scattering and Reflection" *In Preparation.*

18. B.L. Henke, "Low-Energy X-Ray Spectroscopy with Crystals and Multilayers," AIP Conference Proceedings No. 75 on Low Energy X-Ray Diagnostics, Monterey, California, edited by

D.T. Attwood and B.L. Henke (American Institute of Physics, New York, 1965), p. 85.

19. B.L. Henke, R.C.C. Perera, E.M. Gullikson and M.L. Schattenburg, "High-Efficiency Low-Energy X-Ray Spectroscopy in the 100-500 eV Region," *J. Appl. Phys.* 49, 480 (1978).

20. B.L. Henke and M.A. Tester, "Techniques of Low-Energy X-Ray Spectroscopy," *Adv. X-Ray Anal.* 18, 76 (1975).

21. E.M. Gullikson, "Determination of Low Energy X-Ray Optical Constants and Atomic Scattering Factors from Multilayer Reflectivity Measurements". In preparation.

22. The experimental R-values for Mica were determined by B.L. Henke and J. Kerner, Center for X-Ray Optics (1987).

23. D.M. Barrus, R.L. Blake, H. Felthauser, E.E. Fenimore, and A.J. Burek, "Spectrometric Properties of Crystals for Low-Energy X-Ray Diagnostics," AIP Conference Proceedings No. 75 on Low Energy X-Ray Diagnostics, Monterey, California, edited by D.T. Attwood and B.L. Henke (American Institute of Physics, New York, 1982), 115.

24. The experimental R-values were determined by B.L. Henke and R.E. Tackaberry, Center for X-Ray Optics (1985).

25. The sputtered multilayers that have been characterized and compared in the investigation reported here have been constructed at this Center for X-Ray Optics (J.H.Underwood and J. Kortwright), at the Materials Science Laboratory, Stanford University (T. W. Barbee) and at Ovonic Synthetic Materials C., Troy, Michigan (J.L. Wood). Multilayers from the latter two sources have been kindly loaned to this project by the x-ray diagnostics group, P14, of the Los Alamos National Laboratory.

26. B.L. Henke, S.L. Kwock, J.Y. Uejio, H.T. Yamada and G.C. Young, "Low-Energy X-Ray Response of Photographic Films. I. Mathematical Models," *J. Opt. Soc. Am. B* 1, 818 (1984).

27. B.L. Henke, F.G. Fujiwara, M.A. Tester, C.H. Dittmore and M.A. Palmer, "Low-Energy X-Ray Response of Photographic Films. II. Experimental Characterization," *J. Opt. Soc. Am. B* 1, 828 (1984).

28. B.L. Henke, J.Y. Uejio, G.F. Stone, C.H. Dittmore, F.G. Fujiwara, "High Energy X-Ray Response of Photographic Films. Models and Measurements," *J. Opt. Soc. Am. B* 3, 1540 (1986).

29. L. Kissel, R. H. Pratt and S. C. Roy, *Phys Rev A* 22, 1970 (1980).

30. A. Oren, B. L. Henke and E. M. Gullikson, "Program XTALFIT:Calculates Reflection from Multilayer Analyzers Using the Modified Darwin-Prins Model," LBL Report LBID-1399 (April 1988).

31. J.B. Kortright, P. Plag, R. C. C. Perera, P.L. Cowan, D. W. Lindle, and B. Karlin, "Multilayer-Coated Mirrors as Power Filters in Synchrotron Beamlines," LBL Report 24000 (July 1987).

32. J. B. Kortright and R. S. DiGenaro, "Multilayer Mirrors as Power Filters in Insertion Device Beamlines," LBL Report-25803 (August 1988).

33. B. L. Henke "Ultrasoft X-Ray Reflection, Refraction and Production of Photoelectrons (100-1000 eV Region), *Phys. Rev. A* 6, 94 (1972).

34. R.W.G. Wyckoff, *Crystal Structures*, New York, Interscience Publishers (1960).

35. *International Tables for X-Ray Crystallography*, published for the International Union of Crystallography by D. Reidel Pub. Co. (1983).

36. H.T. Yamada, J.C. Davis, B.L. Henke and E.M. Gullikson, "Reflectivity of Fifteen Practical X-ray Analyzer Crystals for the 100-10,1000 eV Region". *In preparation*.

37. I. Langmuir, "Overturning and Anchoring of Monolayers," *Science* 87, 493 (1938).

38. E.P. Honig, "Molecular Constitution of X- and Y- Type Langmuir Blodgett Films" *Journal of Colloid and Interface Science*, 43, 66 (1973).

39. The construction parameters in Table F1 are based upon an analysis of about ten years of experimental results (1975-1985, while this project was located at the Department of Physics - University of Hawaii). We are pleased to acknowledge the collaboration (1985) in this analysis by our post-doctoral physical chemist associate, N.S. Balakrishnam (present address, University of Guam).

40. E. Spiller, "Evaporated Multilayer Dispersion Elements for Soft X-Rays" in *Low Energy X-Ray Diagnostics 1981* D.T. Attwood and B.L. Henke, Eds., AIP Proc. Vol. 75, 125 (1981).

41. T.W. Barbee, Jr., " Sputtered Layered Synthetic Microstructure (LSM) Dispersion Elements" in *Low Energy X-Ray Diagnostics 1981* D.T. Attwood and B.L. Henke, Eds., AIP Conf. Proc. No. 75 (1981).

42. M. Yamamoto, A. Arai, M. Watanabe, and T. Namioka,

"Multilayer Structures and Laboratory X-Ray Laser Research," *Proc. of the SPIE* Vol. 688, 99 (1986).

43. S.V. Gaponov, S.A. Gusev, B.M. Luskin, N.N. Salashchenko, E.S. Gluskin, "Long-Wave X-Ray Radiation Mirrors," *Optics Comm.* 38, 7 (1981).

LAWRENCE BERKELEY LABORATORY
TECHNICAL INFORMATION DEPARTMENT
1 CYCLOTRON ROAD
BERKELEY, CALIFORNIA 94720